©2022 Society of Economic Geologists, Inc.
Economic Geology, v. 117, no. 4, pp. 853–874

Geochemical Data Analysis of Iron Oxide Copper-Gold Mineralization, Wirrda Well Prospect, South Australia

Marija Dmitrijeva,[1,†] Cristiana L. Ciobanu,[1] Kathy Ehrig,[2,3] Nigel J. Cook,[3] Max R. Verdugo-Ihl,[1] Andrew V. Metcalfe,[4] Vadim S. Kamenetsky,[5] Jocelyn McPhie,[5] and Mick Carew[2]

[1] *School of Chemical Engineering and Advanced Materials, The University of Adelaide, Adelaide, South Australia 5005, Australia*

[2] *BHP Olympic Dam, Adelaide, South Australia 5001, Australia*

[3] *School of Civil, Environmental and Mining Engineering, The University of Adelaide, Adelaide, South Australia 5005, Australia*

[4] *School of Mathematical Sciences, The University of Adelaide, Adelaide, South Australia 5005, Australia*

[5] *School of Natural Sciences and Centre of Excellence in Ore Deposits (CODES), University of Tasmania, Hobart, Tasmania 7001, Australia*

Abstract

Multivariate statistical analysis encompasses a range of methods that can fingerprint mineralization, alteration, and host-rock signatures within an ore system, thus assisting in interpretation of ore deposit models and supporting exploration programs. We utilize numeric interpolation of metals (Fe, Cu, and U), principal component analysis (PCA), and a Random Forest (RF) classification, applied to whole-rock geochemical data, to define metal distribution patterns and geochemical signatures of alteration/Fe oxide mineralization in the Wirrda Well iron oxide copper-gold (IOCG) prospect. The prospect is located in the Olympic Dam district, Gawler Craton (South Australia), bounded by NW- and NE-trending faults and characterized by two distinct residual gravity anomalies: Wirrda Well North (WW-North) and Wirrda Well South (WW-South). The mineralization is attributed to hydrothermal activity associated with magmatism at ~1.6 Ga that generated the Gawler Silicic Large Igneous Province (SLIP), corroborated by U-Pb dates of hematite. The mineralization is hosted by the ~1.85 Ga Donington Granitoid Suite and abundant mafic dikes, the majority of which are considered to predate mineralization.

Five lithogeochemical clusters are defined from PCA, hierarchical, and *k*-means clustering, efficiently discriminating least-altered felsic lithologies from altered, mixed lithologies (felsic and mafic) and, importantly, two distinct mineralization clusters, representing magnetite and hematite. The RF method is successfully applied to a larger data set with a smaller number of analyzed elements to extrapolate the results over the whole prospect. WW-North is characterized by an Fe-V-Ni-Co signature defined as "magnetite-type," whereas WW-South contains higher-grade Cu-Au(± Bi-Ag) mineralization and has a marked Mo-W-U(± Sn) signature defined as "hematite-type." The latter is considered a characteristic hypogene hydrothermal signature in the Olympic Dam District. Sodic and hydrolytic alteration are associated with Fe metasomatism and are depicted by the magnetite and hematite clusters, respectively. In combination, the results indicate that premineralization mafic dikes provided permeable structures for fluid focusing and metal deposition, since metals are concentrated by their contacts with host granite, specifically in WW-North. The metal interpolations and geochemical data analysis suggest strong lithological-structural control on IOCG mineralization at Wirrda Well.

Introduction

Whole-rock multivariate geochemical data sets of various types and complexities represent sources of information that can aid characterization and genetic modeling of hydrothermal ore deposits. This is because the geochemical signatures of host lithologies, alteration assemblages, and mineralization can be readily underpinned by multivariate analysis of geochemical data, which, in turn, reflects the mineralogy and mineral assemblages of an ore system (e.g., Halley, 2020). A multivariate statistical approach is especially powerful when trying to identify pathfinder elements that are not themselves economic components of a given deposit yet are persistently and/or systematically associated with the commodity metals, and thus potentially indicate the fertility of ore systems (e.g., Hood et al., 2019). Classification techniques are particularly valuable in cases when a full analytical element suite could not be readily obtained, requiring the extrapolation of predefined classes (e.g., lithology, alteration assemblage) onto a larger geochemical data set with a smaller number of measured elements or other variables (e.g., Ordoñez-Calderón and Gelcich, 2018). Several case studies focus on the statistical analysis of geochemical data to predict lithological classes (e.g., Bérubé et al., 2018; Caté et al., 2018), to map alteration in an individual ore deposit (e.g., Ordóñez-Calderón and Gelcich, 2018), or to map a specific geologic terrane (e.g., Kuhn et al., 2019, 2020). A significantly larger number of recent studies have focused on the mineral chemistry of specific components of ore systems (e.g., Winderbaum et al., 2012; O'Brien et al., 2015; Hart et al., 2017; Gregory et al., 2019; Huang et al., 2019), in part due to the accelerated development and growing availability of microanalytical instrumentation required for rapid acquisition of quantitative trace element data sets. In contrast, application of statistical analysis to large, multielement, whole-rock assay data sets from ore systems is scarce in the published literature, likely due to the proprietary nature of such data sets.

Overall, multivariate statistical methodologies are not novel, yet, to date, there are relatively few such studies that directly characterize alteration, mineralization, and/or the spec-

†Corresponding author: e-mail, dmitrijeva.maria@gmail.com

ISSN 0361-0128; doi:10.5382/econgeo.4904; 22 p.
Digital appendices are available in the online Supplements section.

Submitted: December 14, 2019/Accepted: September 16, 2021

Downloaded from http://pubs.geoscienceworld.org/segweb/economicgeology/article-pdf/117/4/853/5581376/4904_dmitrijeva_et_al.pdf
by China Geological Library user

tral signature of ore systems, and fewer still that specifically target iron oxide copper-gold (IOCG) systems. This is despite the fact that such signatures, if well defined for specific geologic provinces, can enhance the overall understanding of ore genesis and underpin new approaches to mineral exploration.

IOCG deposits are characterized by the presence of magnetite and hematite as major minerals paragenetically associated with Cu-Au ores (Barton, 2014, and references therein). Although either of the Fe oxides can be dominant, commonly, both Fe oxides and their interconversion products are present throughout a given IOCG deposit or province, e.g., the Cloncurry district (Queensland, Australia; Mark et al., 2006), the Great Bear magmatic zone (Northwest Territories, Canada; Corriveau et al., 2016), or the Olympic Dam district (South Australia; Fig. 1; Ehrig et al., 2012, 2017; Verdugo-Ihl et al., 2017, 2020a, b, 2021; Dmitrijeva et al., 2019a, b; Courtney-Davies et al., 2019, 2020a).

The Olympic Cu-Au Province is a world-class IOCG terrane located along the eastern margin of the Gawler Craton, South Australia (Skirrow et al., 2007). This metallogenetic province hosts several dozen deposits and prospects, including the Olympic Dam Cu-U-Au-Ag deposit, represented by different mineralization styles (e.g., breccias, veins, and skarns) and hosted by various basement rocks, including granitoids of different ages and metasedimentary and volcanic rocks. The IOCG event is associated with the Gawler Silicic Large Igneous Province (SLIP) at ~1.6 Ga, comprising Hiltaba Suite intrusions and their cogenetic equivalents, the Gawler Range Volcanics (GRV; Blissett et al., 1993; Allen et al., 2008).

Despite such a wide diversity, deposits/prospects in the Olympic Cu-Au Province share geochemical and mineralogical characteristics, including (1) regional- and deposit-scale alkali-calcic alteration (Conor et al., 2010; Kontonikas-Charos et al., 2014, 2017, 2018; Mauger et al., 2016; Dmitrijeva et al., 2019a, b) and (2) preservation of hypogene U-(Pb)-W-Sn-Mo–bearing, oscillatory zoned hematite typifying the ~1.6 Ga event throughout the Olympic Cu-Au Province (Ciobanu et al., 2013; Verdugo-Ihl et al., 2017; Courtney-Davies et al., 2019, 2020b).

In the Acropolis prospect, a multivariate statistical approach (clustering, classification, and principal component analysis [PCA]) combined with a 3-D geologic model applied to a whole-rock data set (4,864 samples) showed an offset between distribution of weakly mineralized rocks (Cu >200 ppm) and Fe-rich veins, thus supporting a genetic model in which Cu-bearing mineralization overprints Cu-Au–deficient, magnetite-dominant veins (Dmitrijeva et al., 2019b). Moreover, the distinct "magnetite" (Fe-V-Ni-Co) and "hematite" (rare earth element [REE]-W-Sn-Sb-U-Th-Ca-P) signatures recognized at Acropolis (Dmitrijeva et al., 2019b) provide a geochemical model for constraining a transition from early magnetite to late hematite in other IOCG prospects, including Wirrda Well (Fig. 1), where Cu-Au mineralization is associated with both Fe oxides.

Multivariate statistical analysis of data from both Olympic Dam and Acropolis have shown that the geochemical signatures defining mineralization (Fe-Cu-Au ± U) include W, Mo, Sn, and As (Dmitrijeva et al., 2019a, b), a set of elements which are inconsistently associated with IOCG mineralization in terranes elsewhere. Enrichment in U has, however, been recognized as part of the geochemical signature associated with potassic/iron alteration in mineralization from the Great Bear magmatic zone, Canada (Montreuil et al., 2013). The trace elements W, Mo, Sn, and U are typical of U-(Pb)-W-Sn-Mo–zoned hematite in all studied IOCG systems in the Olympic Dam district (Verdugo-Ihl et al., 2017; Courtney-Davies et al., 2020a). The U-(Pb)-W-Sn-Mo signature (hereafter called "granitophile") is considered to signify a granitic affiliation relating to incorporation of these elements within the crystal structure of hypogene hematite (Ciobanu et al., 2013, 2018; Verdugo-Ihl et al., 2020a).

Here, we use numeric interpolation of metals combined with extended multivariate statistical analysis applied to whole-rock geochemical data sets to define metal distribution patterns at Wirrda Well and the geochemical signatures of alteration and mineralization. This enables comparison with other IOCG systems in the district studied by comparable analytical methods. The objective of this comparison is to understand how differences in local geologic setting are reflected in whole-rock geochemical data. Numeric interpolations of Fe, Cu, and U in Wirrda Well and statistical analysis of whole-rock geochemical data highlight the importance of the local setting in focusing fluids and providing traps for mineralization. The quantitative approach, with the aim of pulling apart geochemical signatures of mineralization and alteration, is important for optimization and implementation of exploration programs in the Olympic Cu-Au Province and IOCG terranes elsewhere.

Geologic Background

The geologic domains hosting the Olympic IOCG Province comprise reworked terranes that were accreted to the Meso- to Neoarchean nucleus of the Gawler Craton in the Paleoproterozoic (Betts and Giles, 2006). IOCG mineralization in the Olympic Province is attributed to a short-lived episode of north-northwest–south-southeast extension that approximately coincided with GRV eruption that was both preceded and followed by more protracted northwest-southeast to north-northwest–south-southeast contraction (Hayward and Skirrow, 2010). The mantle-crustal IOCG model introduced by Groves et al. (2010) is consistent with recent lithospheric reconstructions for the Olympic Province, whereby delamination of metasomatized (fertilized with volatiles and ore elements) subcontinental lithospheric mantle during the SLIP event is followed by bimodal magmatism and mineralization in a back-arc environment (Skirrow et al., 2018).

The Olympic Dam IOCG district hosts the Olympic Dam Cu-Au-Ag-U deposit and satellite prospects such as Acropolis and Wirrda Well. Olympic Dam (Fig. 1) is a hematite-dominant IOCG deposit entirely enclosed within a breccia complex formed mostly from alteration of the Hiltaba Suite Roxby Downs Granite (Reeve et al., 1990). Well-defined zonation of Cu(-Fe) sulfide minerals from pyrite-chalcopyrite through chalcopyrite-bornite to bornite-chalcocite towards central and shallower levels is recognized from mineralogical-geochemical data sets (Ehrig et al., 2012, and references therein). The concentric zonation was reproduced by only one (Cu-U_3O_8-Se-S) of the two geochemical associations that form part of the IOCG signature as defined by statistical analysis (principal component analysis on centered log ratio (clr)-

Downloaded from http://pubs.geoscienceworld.org/segweb/economicgeology/article-pdf/117/4/853/5581376/4904_dmitrijeva_et_al.pdf
by China Geological Library user

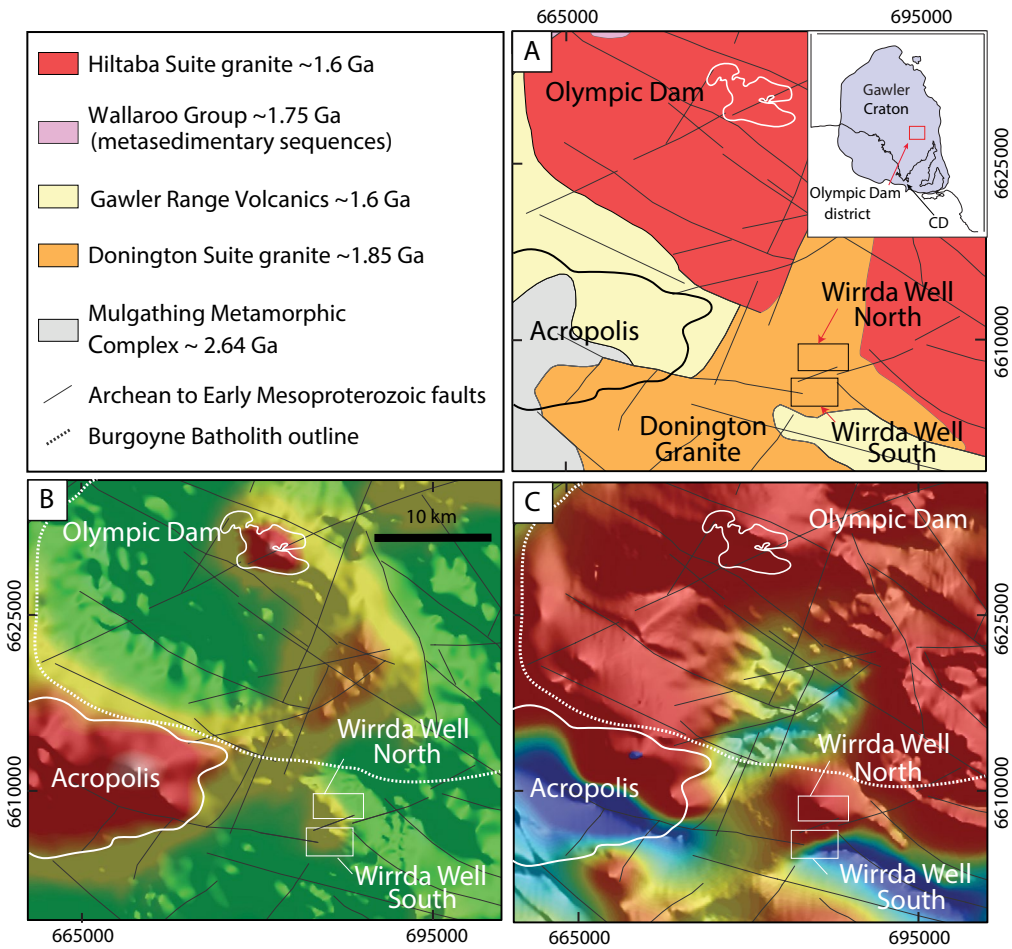

Fig. 1. (A) Geologic map of the basement in the Olympic Dam district showing the location of the Wirrda Well and Acropolis prospects relative to the Olympic Dam district. (B) Bouguer gravity and (C) total magnetic intensity (TMI) maps. Color scale is red for positive/highest and green/blue for negative/lowest intensities. Note large gravity response of Acropolis (black outline) relative to other IOCG prospects. The approximate outline of the Burgoyne Batholith (white dashed line) is interpreted from potential field anomalies and Ehrig (2013). Maps sourced from https://map.sarig.sa.gov.au. Abbreviation: CD = Cape Donington.

transformed data coupled with hierarchical clustering) of a large data set (10,565 samples). The second association (Au-W-Mo-Sb-As) defines a vertical ~1,800-m-deep corridor in the southeastern lobe of the deposit (Dmitrijeva et al., 2019a).

In contrast, Acropolis, a prospect ~25 km southwest of Olympic Dam (Fig. 1) comprises veins and stockworks predominantly hosted within felsic GRV rocks (Paterson, 1986; Creaser, 1989; Cross, 1993; McPhie et al., 2020). Recent petrological and geochemical studies of fluorapatite and Fe oxides, U-Pb dating of hematite, and statistical analysis of whole-rock data sets defining mineralization and alteration footprints at Acropolis (Krneta et al., 2017a; Cherry et al., 2018; Courtney-Davies et al., 2019; Dmitrijeva et al., 2019b; Verdugo-Ihl et al., 2021) enabled the prospect to be unequivocally tied to ~1.6 Ga IOCG metallogeny in the Olympic Dam district.

The Wirrda Well prospect, ~25 km south-southeast from the Olympic Dam deposit (Fig. 1), is hosted by variably deformed megacrystic alkali feldspar granites of the Donington Granitoid Suite (hereafter referred to as Donington granite) emplaced at ~1850 Ma (Jagodzinski, 2005). Exploration diamond drilling at Wirrda Well defined two zones of mineralization, Wirrda Well North and Wirrda Well South (hereafter WW-North and WW-South), which are characterized by the presence of magnetite in addition to hematite, as well as the presence of numerous mafic dikes (Cross, 1993; Ehrig, 2013; Fig. 2).

Within the broader tectonomagmatic context of the eastern Gawler Craton, Hayward and Skirrow (2010) interpreted Wirrda Well as one of several deposits formed along ENE- to NE-trending extensional faults near their intersections with major NNW- to NW-trending faults in the hanging wall of first-order terrane boundary faults (Fig. 2A). The oldest lithology at Wirrda Well is the ~1.85 Ga Donington granite emplaced during a compressional event termed the Cornian orogeny. This was followed by an extensional regime during which a suite of mafic dikes, the Tournefort Metadolerite, were emplaced into the Donington Suite at ~1815 Ma (Reid et al., 2008a, and references therein). Deformation of Donington granite is attributed to the 1.73 to 1.69 Ga Kimban orogeny with greenschist to granulite facies metamorphism reported from different domains across the Gawler Craton

Downloaded from http://pubs.geoscienceworld.org/segweb/economicgeology/article-pdf/117/4/853/5581376/4904_dmitrijeva_et_al.pdf
by China Geological Library user

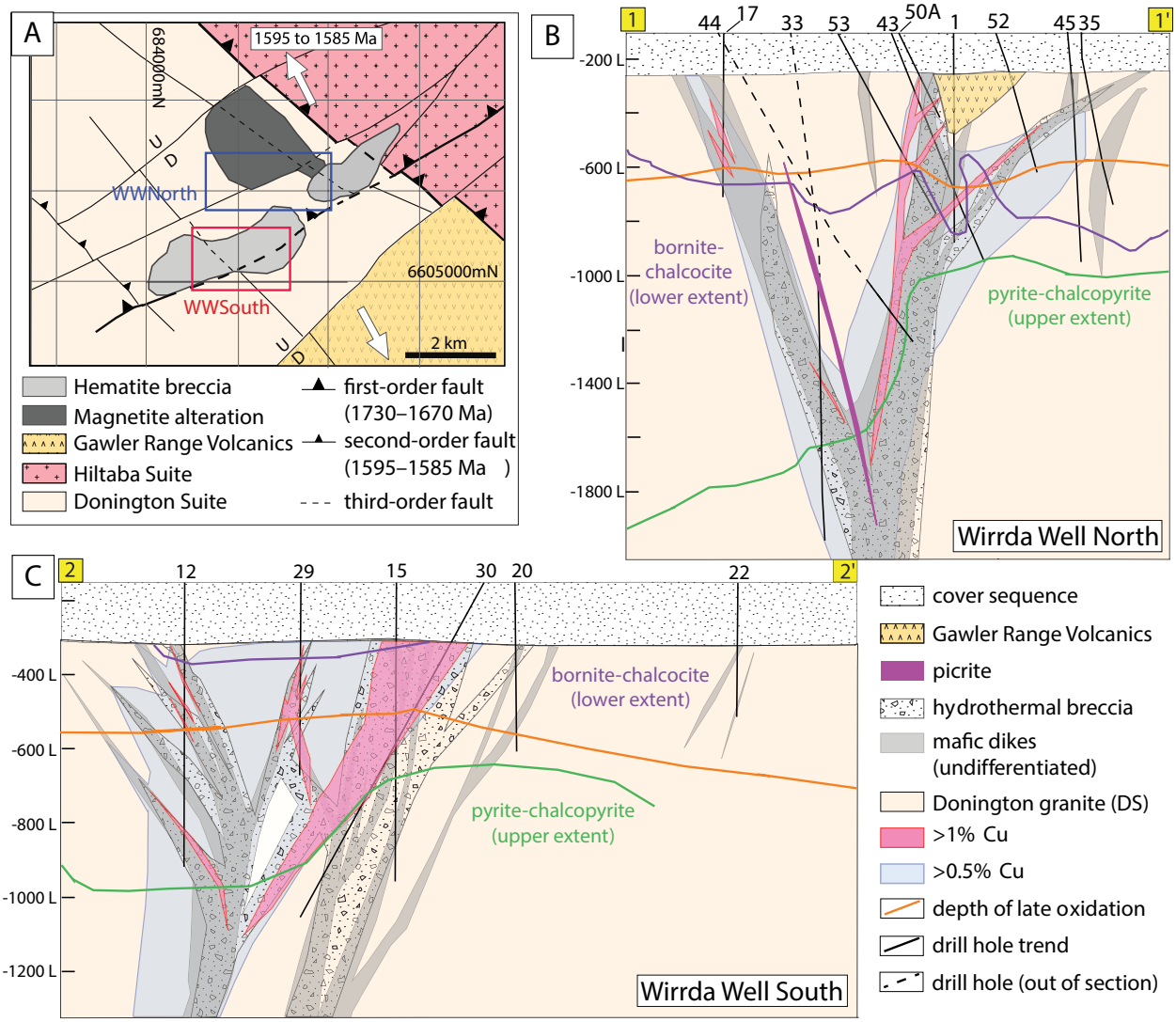

Fig. 2. (A) Geologic sketch map of basement (adapted from Hayward and Skirrow, 2010) and schematic cross sections of WW-North (B) and WW-South (C), after Ehrig (2013). Schematic cross sections are marked on map on Figure 3A.

(e.g., Reid et al., 2008b). Unaltered Donington Suite granite from the Eyre Peninsula comprises various leuco- and melanocratic varieties and subordinate migmatites (Reid et al., 2008a; Kontonikas-Charos et al., 2018; Keyser et al., 2019). At Cape Donington (Lincoln National Park, Eyre Peninsula), the Donington Suite is crosscut by younger, pyroxene-rich dolerite dikes emplaced during the Kimban orogeny ($^{206}Pb/^{238}U$ weighted mean age of 1711 ± 14 Ma; SHRIMP zircon dating; Keyser et al., 2020). The northern limb of the Donington Suite, occurring in the Wirrda Well area, is crosscut by numerous mafic dikes, the ages of which remain unconstrained (Fig. 2B, C).

Mineralization at Wirrda Well, initially considered to be hosted within a single granitic breccia body (Parker, 1990), was later related to subvertical "hydrothermal breccia" bodies (Fig. 2B, C; Ehrig, 2013). The predominantly subvertical mafic dikes vary from a few centimeters to several meters in width and range from undeformed to foliated and mylonitized, as well as brecciated. Mineralized zones (>1% Cu) are placed at the contacts between dikes and host granite, albeit as narrow zones in WW-North and wider zones in WW-South (Fig. 2B, C). The given subvertical dips of mafic dikes were interpreted based on examination of drill core from the BHP exploration team (Fig. 2B, C). This drill core logging-based model shows that mineralized zones are defined by cutoffs of ≥1% Cu content, whereas the weaker mineralized areas are defined by Cu content in the 0.5 to 1.0% Cu range. As seen from the cross sections (Fig. 2B, C), the brecciated rocks hosting mineralization defined as "hydrothermal breccias" extend as narrow zones encompassing both granite and mafic dikes, lithologies that are still recognizable. Picrites crosscut mineralization, are relatively unaltered, and contain "fresh" biotite as well as olivine (Ehrig, 2013). The prospect is comparable with Acropolis in that the dominant mineralization comprises a chalcopyrite + pyrite assemblage associated with magnetite + hematite, but with a shell of bornite + chalcocite + hematite at upper levels close to, yet still below, the supergene oxidation boundary (Fig. 2B, C; Ehrig, 2013).

Downloaded from http://pubs.geoscienceworld.org/segweb/economicgeology/article-pdf/117/4/853/5581376/4904_dmitrijeva_et_al.pdf
by China Geological Library user

Geochemical signatures of fluorapatite from Wirrda Well and Acropolis record a comparable transition from early magnetite to late hematite stages resembling those reflecting the magmatic to hydrothermal transition at Olympic Dam (Krneta et al., 2017a, b). U-Pb dating of zoned hematite has yielded a mineralization age of 1598.9 ± 6.3 Ma (drill hole WRD46; Courtney-Davies et al., 2019). Magmatic alkali-feldspars and plagioclase are preserved in Donington granite from the location providing the dated hematite, albeit with superimposed albite + sericite + hematite alteration in other parts of the prospect (Kontonikas-Charos et al., 2018; Krneta et al., 2017a).

Lithologies and Data Sets

The Wirrda Well prospect is intersected by 48 drill holes (Fig. 3) under Late Proterozoic Stuart Shelf sedimentary rocks of thickness between 350 and 600 m. The potential field anomalies are nearly coincident with gravity (6 mGal) and magnetic highs (1,800 nT) (Fig. 1; Vella, 1997).

Despite alteration, distinct lithologies at Wirrda Well are recognizable in hand specimen (Fig. 4A-G). The felsic magmatic rocks, of which ~70% are Donington granite, display coloring and fabrics that make them distinct from one another (Fig. 4A). Unmineralized, pale-pink, medium-grained K-feldspar granite (intersected in drill hole WRD19; Figs. 3, 4A) was attributed to the Hiltaba Suite based on a laser ablation-inductively coupled plasma-mass spectrometry (LA-ICP-MS) U-Pb zircon age yielding 1622 ± 18 Ma (M. Kamenetsky, unpub. data). This is likely a component granite of the Burgoyne Batholith that produces gravity lows towards the northeast (Ehrig, 2013). Minor, felsic GRV rocks are found within both WW-North and WW-South (Figs. 3, 4A).

Mafic dikes of undifferentiated age and provenance, henceforth referred to as "undifferentiated" (~10% of the total; Fig. 4B) are intensively chloritized. Unaltered mafic dikes are separated as dolerites (~2%; Fig. 4B). Unmineralized picrites intersected in drill hole WRD33 (Figs. 2B, 4B; Ehrig, 2013) have a distinct gray-brownish color and are penecontemporaneous with the IOCG event (U-Pb apatite dating yielding an age of 1596 ± 17 Ma; Huang et al., 2016). Mylonites (~4%; Fig. 4C) occur along shear zones in either Donington granite or undifferentiated mafic dikes. The rest of the lithologies comprise massive iron oxide rocks.

Foliation and deformation fabrics are, however, typical of the Donington granite (Fig. 4D-G) as well as at contacts to undifferentiated dikes. Iron oxides occur as clots/patches, segregation bands, or crosscutting veinlets throughout the Donington granite, mylonites, and undifferentiated dikes (Fig. 4E-G).

Whole-rock, multi-element geochemical data for the Wirrda Well prospect consists of two distinct data sets, both collected at 1-m drill core intervals (Fig. 3). These are 1) a larger data set (29,172 samples from all 48 drill holes) analyzed for a "limited element suite" (32 elements analyzed) and 2) a smaller data set (6,155 samples from just 10 of the 48 drill holes) analyzed for an additional "extended" 46-element suite from the same set of samples as in the limited element suite data set. These two data sets are almost non-overlapping, because an element present in one data set will be either only partially or not measured at all in the other, or below its respective minimum limit of detection (Table 1). Each whole-rock sample within the limited element suite was analyzed at Bureau Veritas (Adelaide), whereas the extended element suite analyses were completed at Intertek/Genalysis (Adelaide). A summary of both data sets with respect to minimum detection limits (mdl), acquisition method, and the proportion of analyses falling below mdl for each element is presented in Table 1.

In order to extract the maximum information from these data, the two data sets were combined to form a joint geochemical data set consisting of 6,155 analyses of 51 elements in 10 drill holes (Table 1). This data set is hereafter referred to as the "compiled suite." To ensure that such a merging of data, when possible, is geochemically valid, a comparison of data from limited and extended suites was made for a range of elements such as Cu, U, Ce, Y, Mo, Sr, Co, Ni, Pb, and Zn (App. 1; Figs. A1, A2). These comparisons show good reproducibility of the data from two different laboratories; however, obvious biases exist between the two data sets at values close to minimum detection limits. Additionally, specific gravity (bulk dry density) and magnetic susceptibility are reported for the majority of the 29,172 samples in the larger data set, thus allowing these parameters to be included in statistical analysis.

Methods

The methods applied in this study consist of implicit numeric interpolation and multivariate statistical analysis, which are described in greater detail in Appendix 1.

The limited element suite is used as input data sets in Leapfrog Geo 5.0 implicit modeling software to obtain numerical modeling for Wirrda Well. Numerical modeling of the continuous variables Cu (ppm), Fe (wt %), and U (ppm) was done using spheroidal kriging with "no drift" in both WW-North and WW-South. The NW-trending and second-order, ENE-trending faults are shown to be associated with Wirrda Well mineralization (Hayward and Skirrow, 2010). Therefore, the regional NW (strike 116°) and ENE trends (strike 73°) were applied for the numeric interpolation in WW-North and WW-South, respectively, because (1) such trends are supported by the regional orientation of the first- and second-order faults, and (2) applying such a trend produces smaller volumes by respecting the space between drill holes and results in realistic metal distributions. Importantly, the ore shells are not moved or shifted due to the applied trend and are thus effectively generated around the corresponding downhole geochemical data.

Multivariate statistical analysis included two different approaches (unsupervised and supervised), each defined by the type of algorithm used to find and constrain geochemical trends. The full description is given in Appendix 1, and a summary of the workflow is presented in Figure 5.

The unsupervised approach comprises variation matrix, hierarchical dendrogram, k-means clustering, and principal component analysis and aims to identify patterns in the compiled suite. This is carried out using the computing algorithm without predefined categories, allowing an unbiased identification of sets of elements defining geochemical associations (groups) or set of samples linked to such associations (clusters). The variation matrix depicts an association between each pair of elements, hierarchical dendrograms define geo-

Downloaded from http://pubs.geoscienceworld.org/segweb/economicgeology/article-pdf/117/4/853/5581376/4904_dmitrijeva_et_al.pdf
by China Geological Library user

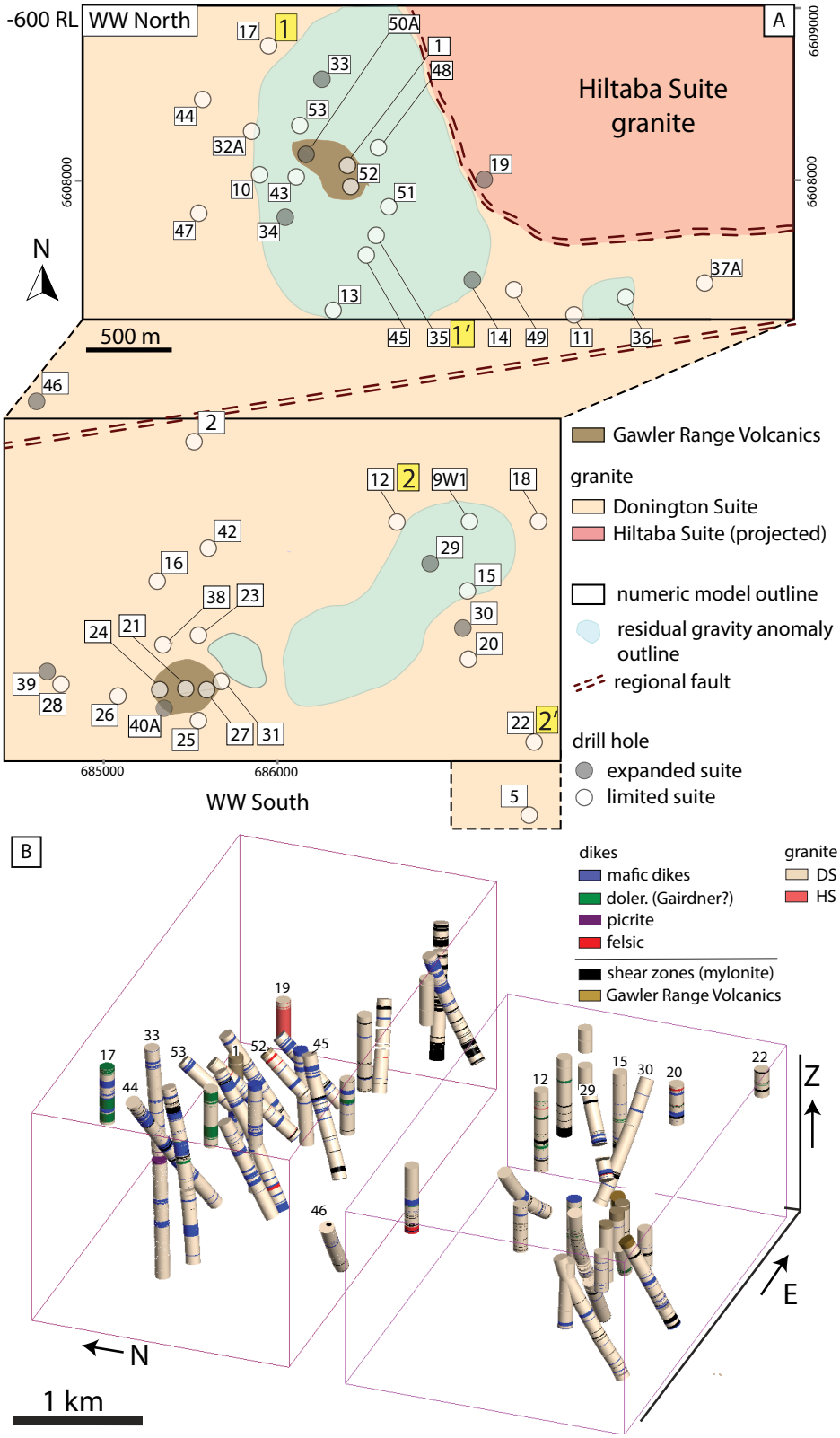

Fig. 3. Geologic sketch map (A) of WW-North and WW-South showing locations of the 48 "WRD" drill holes (boxed numbers), colored by the corresponding geochemical data suite. Approximate location and trace of regionally identified faults is indicated in Figures 1A and 2A. Residual gravity anomaly outlines are from Ehrig (2013). Locations of cross sections 1-1' and 2-2' on Figure 2B and C are given. (B) The 48 "WRD" drill holes with logging data downhole, showing abundance of mafic dikes, especially in the WW-North, dolerite, shear zones/mylonite zones, hosting lithology, Donington Granite, and unconformable Gawler Range Volcanics (see Fig. 4A-G).

Downloaded from http://pubs.geoscienceworld.org/segweb/economicgeology/article-pdf/117/4/853/5581376/4904_dmitrijeva_et_al.pdf
by China Geological Library user

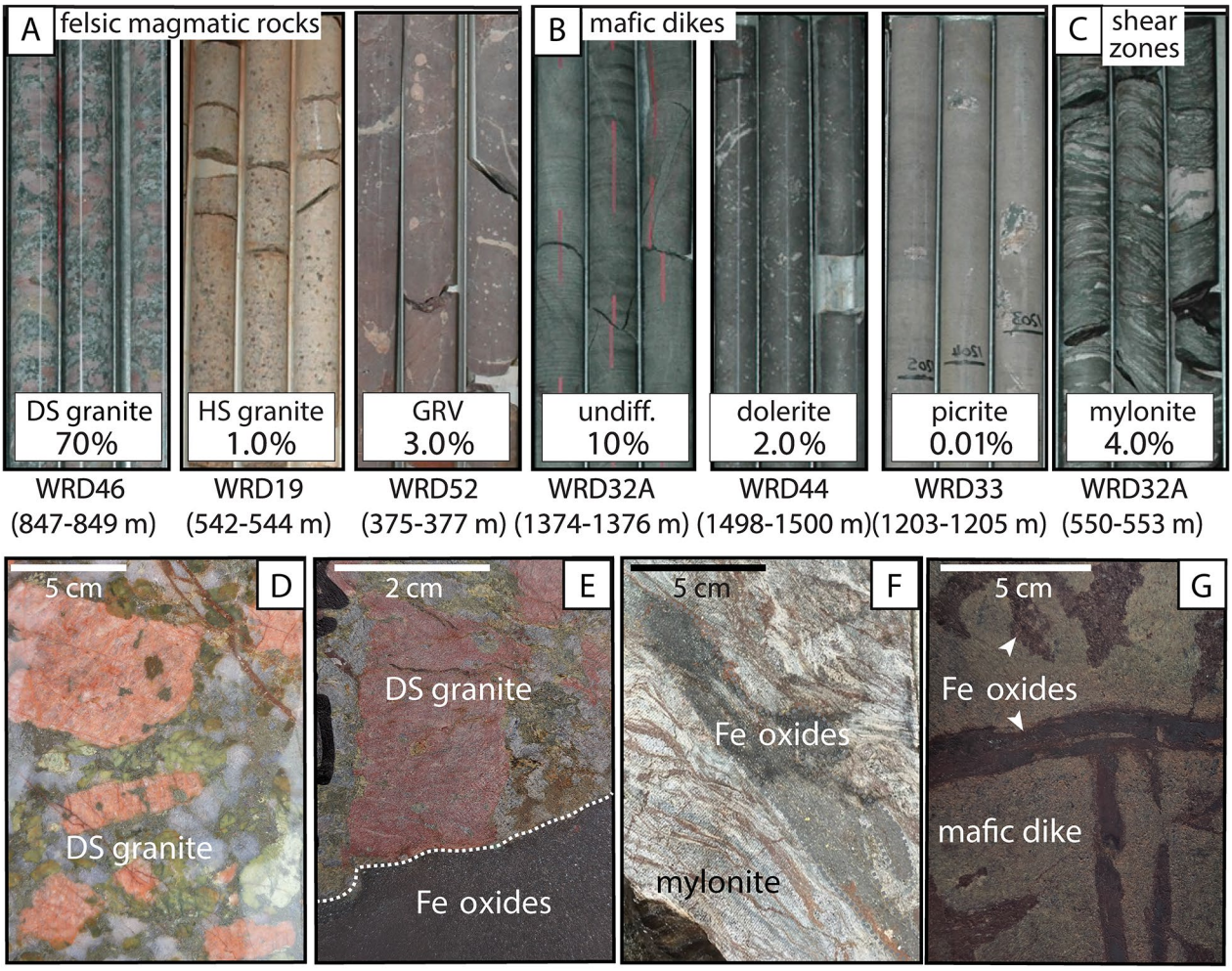

Fig. 4. (A-G) Photographs of representative lithologies from the selection of 1-m drill cores from the Wirrda Well prospect as marked. Percentages (as per core logging) represent proportions of these lithologies in the whole-rock data set. (D-G) Photographs of representative hand specimens: (D) Least-altered DS granite—note the yellow-green alteration of plagioclase; (E, F) Fe oxides within and along microshears in altered and mylonitized DS, respectively; (G) Fe oxide-bearing veinlets within undifferentiated mafic dike. Abbreviations: DS = Donington Suite granite; GRV = Gawler Range Volcanics; HS = Hiltaba Suite.

chemical groups, and k-means clustering determines the geochemically similar clusters of samples. Principal component analysis provides an assessment of relationships between groups of elements and clusters of samples, thus leading to identification of the geochemical signatures corresponding to each cluster.

The supervised approach, using the Random Forest (RF) classification algorithm (Breiman, 2001; Liaw and Wiener, 2002), allows clusters defined by the unsupervised approach to be extrapolated to the limited element suite. Predicting cluster membership for this larger suite allows each sample to be assigned to a specific cluster that may represent host lithology, alteration, or mineralization. Thus, the supervised approach overcomes the absence of certain elements in the larger data set for which accurate measurement is lacking (e.g., W, Mo, Sn, Bi, As, Sb, and Ag) but which are nevertheless critical for defining IOCG signatures in the district (Dmitrijeva et al., 2019a, b). Full descriptions of multivariate statistical methodology are given in Appendix 1.

Results

3-D metal distributions

The downhole logging data show that undifferentiated mafic dikes form dense swarms within WW-North and become less abundant in WW-South (Fig. 3B; 6B). Geophysical signatures (Ehrig, 2013) and the relative absence of dikes within the body of the unroofed Hiltaba Suite granite in the northeast part of the prospect (Fig. 6) were taken to represent a "terrane boundary" in the Hayward and Skirrow (2010) model for Wirrda Well.

Numerical distribution models for Cu in WW-North and WW-South are presented in a plan view at –600 RL (relative to sea level) and in a vertical cross section, A-A' (Fig. 6). Outlines of >15 wt % Fe and >50 ppm U are projected as dashed lines on these figures to highlight patterns of metal concentration. In plan view, Cu values and Fe outlines are seen to be somewhat comparable in WW-North and -South but with differences at depth (Fig. 6).

Downloaded from http://pubs.geoscienceworld.org/segweb/economicgeology/article-pdf/117/4/853/5581376/4904_dmitrijeva_et_al.pdf
by China Geological Library user

Table 1. Elements Represented in the Limited (29,172 samples analyzed for 32 elements) and Extended (6,155 samples analyzed for 33 elements) Suite Data Sets, with Respective Minimum Detection Limits (Mdl) and the Proportion of Values Falling Below Mdl for Each Element

	Limited Suite			Extended Suite		
Element	Mdl (ppm)	% below mdl	Method	Mdl (ppm)	% below mdl	Method
Ag	1 ppm	81	3A/OES	0.1*	10	4A/MS
Al	0.01%*	-	LBF/OES			
As	10 ppm	77	3A/OES	1*	2	4A/MS
Au	0.02 ppm*	46	FAAA			
Ba	0.02%*	13	LBF/OES			
Be				0.5*	-	LBF/MS
Bi	3	60% not measured	LBF/MS	0.05*	0.4	4A/MS
Ca	0.01%*	0.05	LBF/OES			
Cd				0.05*	22	4A/MS
Ce	0.01%	12	LBF/OES	0.5*	-	LBF/MS
Cu	50 ppm*	4	3A/OES	1	86% not measured	4A/OES
Co	5 ppm	3	3A/OES	0.1*	-	4A/MS
CO_2	0.05%*	23	IFS			
Cr	20 ppm*	42				
Cs				0.05*	0.1	LBF/MS
Fe	0.01%*	-	LBF/OES			
Ga				0.1*	-	LBF/MS
Ge				0.1*	3.0	4A/MS
Hf				0.1*	0.1	LBF/MS
In				0.05*	8	4A/MS
K	0.01%*	0.1	LBF/OES			
La	0.005%	10	LBF/OES*	0.2*	-	LBF/MS*
Li				0.1*	-	4A/MS
Lu				0.02*	-	LBF/MS
Mg	0.01%*	0.02	LBF/OES			
Mn	0.01%*	5.4	LBF/OES			
Mo	5 ppm	67	3A/OES	1*	7	LBF/MS
Na	0.01%*	0.2	LBF/OES			
Nb				0.1*	0.6	LBF/MS
Nd				0.1*	-	LBF/MS
Ni	5 ppm	11	3A/OES	1	88% not measured	4A/OES
Pb	10 ppm	49	3A/OES	5	30% not measured	4A/OES
P	0.01%*	1.7	LBF/OES			
Rb				0.1	0.04	LBF/MS
S	0.01%*	9.4	IFS			
Sb	1 ppm	60 % Not measured	LBF/MS	0.5*	13	LBF/MS
Sc	5 ppm*	6.33	LBF/OES			
Se				1*	56	4A/MS
Si	0.01%*	-	LBF/OES			
Sn				1*	0.1	LBF/MS
Sr	20 ppm	6% Not measured	LBF/OES	0.5*	-	LBF/MS
Ta				0.1*	2.9	LBF/MS
Te				0.1*	42	4A/MS
Th	4 ppm	57% Not measured		0.05*	-	LBF/MS
Ti	0.01%	0.3	LBF/OES			
Tl				0.02*	0.03	4A/MS
U[1]	4	2.5	XRF	0.5*	-	LBF/MS
	0.5		LBF/MS			
V	20 ppm*	2.7	LBF/OES			
W				1*	0.22	LBF/MS
Y	5 ppm	60% not measured	LBF/OES	0.5*	-	LBF/MS
Yb				0.05*	-	LBF/MS
Zn	5 ppm*	0.1	3A/OES	1	86% not measured	4A/OES
Zr	20 ppm*	1.3	LBF/OES			

Notes: Values marked with a * indicated those elements used to form the compiled elemental suite (6,155 observations of 51 elements) in 10 drill holes; if the element was not included in the set of elements for all analyses, then the proportion of not-measured instances is indicated

Abbreviations: FAAA = fire assay-flame atomic absorption spectrometry; IFS = induction furnace-infrared spectrometry; LBF/MS = lithium borate fusion and inductively coupled plasma-mass spectrometry (ICP-MS); LBF/OES = lithium borate fusion inductively coupled plasma-optical emission spectroscopy (ICP-OES); 3A/OES = three-acid (i.e., HCl, HNO_3, $HClO_4$) digestion and ICP-OES; 4A/MS = four-acid digestion ICP-MS; 4A/OES = four-acid digestion (i.e., HCl, HNO_3, $HClO_4$, HF) ICP-OES

[1]61% of the U assaying in the Limited Suite was performed by X-ray fluorescence (XRF)—this was changed to LBF/MS during the drilling program; the benefit of changing to LBF/MS was a lower mdl, with no loss of accuracy

Downloaded from http://pubs.geoscienceworld.org/segweb/economicgeology/article-pdf/117/4/853/5581376/4904_dmitrijeva_et_al.pdf
by China Geological Library user

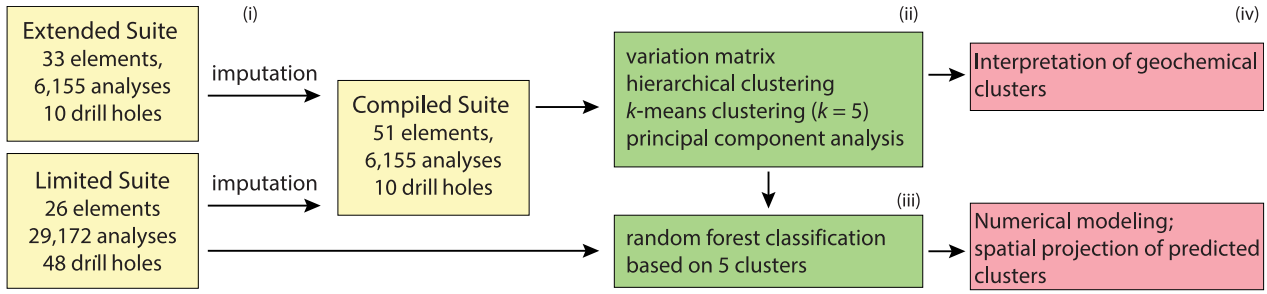

Fig. 5. A four-step workflow diagram showing the sequence of data analysis procedures: (i) imputation of values falling below the minimum detection limit and assembly of compiled suite data; (ii) unsupervised data analysis applied to the compiled suite data; followed by (iii) random forest classification of limited suite data; and (iv) interpretation and visualization of the results.

Copper distributions display notable differences between the two parts of the prospect, with the strongest anomalies (>3,000 ppm Cu) more pronounced and wider in WW-South (Fig. 6). In plan view in WW-South, Cu is also seen to form a broad halo (Fig. 6), thus contrasting with the Cu distribution in WW-North, where the highest Cu concentrations are restricted to a small area relative to the much larger domain of elevated Fe. Evidently, there is a marked mismatch between Cu distribution and very high (>15 wt %) Fe content at WW-South. This is especially notable at depth, where Cu forms a broad halo (Fig. 6).

Concentrations of Fe below 5 wt %, roughly equal to fresh granite, are present throughout the prospect, but not in drill hole WRD19 intersecting the Hiltaba Suite granite. More significant anomalies (>15 wt % Fe) are present in WW-North (Fe contours on Fig. 6), with increasing concentration at depth in WW-North relative to WW-South.

Uranium is present at concentrations that average <100 ppm across the sample suite. In plan-view (U contours on Fig. 6), U shows a distribution broadly comparable to that of Fe and Cu. Background U concentrations (~20 ppm) are present throughout the prospect, including in drill hole WRD19 intersecting the Hiltaba Suite granite. Higher U values (>50 ppm) are located within the >15 wt % Fe outline. The strongest U anomaly (~80 ppm U) is located on the eastern side of WW-South (U contours on Fig. 6).

Multivariate statistical analysis: alteration and mineralization signatures

Definition of geochemical groups: Variation matrix and dendogram: The variation matrix (Table 2; App. 2, Table A1) and hierarchical clustering of elements from the compiled suite shows groups of elements that can be linked to precursor lithology, alteration, and mineralization.

Six groups of elements (groups A-F) are identified on the hierarchical dendrogram (Fig. 7). The CO_2-Mn pair forms a distinct node (group A) on the dendrogram that can be attributed to "carbonates." That is confirmed by the variation matrix, where Mn is the only element which shows the largest proportionality with CO_2 (τ_{MnCO_2} = 1.6), where τ represents the proportionality between any two components, thus suggesting that carbonates are the most significant hosts for Mn. Additionally, CO_2 shows the greatest dissimilarity with the majority of elements defining the Cu-Au-(Ag) ores: Cu (τ_{CuCO_2} = 6); Au (τ_{AuCO_2} = 6. 4); and Ag (τ_{AgCO_2} = 6. 8), and elements forming silicates such as Al (τ_{AlCO_2} = 5.4; τ_{ZrCO_2} = 5.1) (Table 2).

Group B ("felsic rocks") is almost exclusively made up of elements found in rock-forming silicates and accessory minerals. This group can be subdivided into high field strength elements (HFSEs; Nb-Ta-Zr-Hf-Th) and an additional set comprising the element set Si-Al-K-Na-Rb-Ba-Sr-Cs-Tl (Fig. 7). Although we note that elements such as Fe, Ca, Mg, Ti, and P are absent from this group, the association is best fitted to granites, the dominant felsic rocks at Wirrda Well.

Group C ("mafic rocks") comprises the element set Mg-Ti-Cr-Zn-Cd-Li, which can be attributed to (altered) mafic dikes: τ_{CrMg} = 0.7; and τ_{CrTi} = 0.7, τ_{CrSc} = 0.7 (Table 2).

Group D ("magnetite") is composed of Fe-Ni-Co-V-Sc-Ca-P, an association representative of all iron oxides, although the presence of Ni, Co, Ca, and P is indicative of magnetite rather than hematite. We note that such a signature, although obtained from whole-rock analysis of magnetite-rich intervals, will also include variable proportions of elements present in the host lithologies, and therefore, some elements that are depicted here (e.g., Ni) could have been inherited from the mafic dikes. Thus, this is not a geochemical signature of the mineral sensu stricto, which would require assessment by studies dedicated to the magnetite itself, but rather a signature of magnetite in the context of IOCG mineralization from the prospect/district. Other elements, such as Ca and P, which are included in group D, can be explained by the association of magnetite with fluorapatite, a minor but ubiquitous component of magnetite-rich samples at Wirrda Well (Krneta et al., 2017b). Pyrite, which is associated with magnetite at Wirrda Well but is also a major component of chalcopyrite-bearing ores hosted by hematite breccias in other South Australian IOCG deposits, is the main host for Co (and Ni), as shown by multivariate statistical study of a large LA-ICP-MS data set for pyrite from Olympic Dam (Dmitrijeva et al., 2020). This group shows a high degree of proportionality among its members: τ_{FeV} = 0.3; τ_{FeNi} = 0.3; τ_{FeCo} = 0.5; and τ_{CaP} = 0.4.

Group E is one of the largest groups on the dendrogram, and includes a mixed set of elements: W, Sn, various chalcophile elements (As-Sb-Se-In-Ge), but also REEs (Ce-Nd-Y-Yb-Lu), Ga, and Be. This group thus includes elements typically occurring in hematite (Sn and W), but also other elements (REEs or Ga), that have been documented in both Fe oxides in IOCGs across the district (Verdugo-Ihl et al., 2017, 2020a; Courtney-Davies et al., 2019). Group E is therefore

Downloaded from http://pubs.geoscienceworld.org/segweb/economicgeology/article-pdf/117/4/853/5581376/4904_dmitrijeva_et_al.pdf
by China Geological Library user

Table 2. Variation Matrix (submatrix) of 31 Elements from the Compiled Suite Data

	Ag	Al	As	Au	Bi	CO_2	Cu	Co	Cr	Fe	K	Li	Mn	Mo	Na	Nb	Ni	S	Sc	Sb	Se	Si	Sn	Ta	Te	Th	Ti	U	V	W
Al	2.6																													
As	1.9	1.4																												
Au	2.0	2.8	2.0																											
Bi	2.5	2.9	1.8	2.6																										
CO_2	6.8**	5.2**	4.7	6.4**	5.5**																									
Ce	1.7	1.0	1.1	1.7	2.4	5.1**																								
Cu	1.8	3.1	2.4	2.1	2.0	6.0**																								
Co	2.1	1.4	0.8	2.1	2.3	4.5	2.2																							
Cr	2.7	1.0	1.4	2.7	3.1	5.5**	3.0	1.4																						
Fe	1.6	1.5	0.7	1.8	2.4	4.3	2.0	0.5	1.4																					
K	3.3	0.2*	2.2	3.6	4.0	6.1**	4.1	2.2	1.4	2.3																				
Li	2.1	0.3	1.1	2.2	2.6	5.3**	2.4	0.9	0.7	1.0	0.7																			
Mn	4.1	2.4	2.3	3.8	3.5	1.6	3.4	1.7	2.6	1.7	3.2	2.2																		
Mo	1.8	1.8	1.4	2.1	2.2	5.7**	1.8	1.5	2.1	1.1	2.5	1.3	3.0																	
Na	2.6	0.4	1.4	2.7	3.1	5.6**	3.4	1.7	1.2	1.6	0.6	0.7	2.8	2.0																
Nb	2.4	0.5	1.4	2.5	2.9	5.2**	3.0	1.5	1.5	1.4	0.7	0.7	2.5	1.8	0.6															
Ni	2.1	1.3	1.1	2.3	3.0	4.5	2.5	0.4	1.1	0.3	2.0	0.8	1.7	1.6	1.5	1.5														
S	3.4	3.9	3.1	3.5	3.7	5.0**	1.9	2.0	3.8	1.9	4.9	3.1	2.6	2.7	4.5	3.5	2.0													
Sc	2.0	0.6	0.8	2.3	2.7	4.5	2.5	0.6	0.7	0.5	1.1	0.3	1.7	1.3	0.8	0.9	0.4	2.7												
Sb	1.7	1.1	0.6	1.9	2.1	4.1	2.3	0.8	1.2	0.5	1.8	0.9	1.8	1.3	1.2	1.1	0.7	2.7	0.6											
Se	1.7	0.8	1.0	1.9	2.6	4.8	2.4	0.8	1.2	0.7	1.3	0.6	2.2	1.4	0.9	0.8	0.7	2.7	0.5	0.7										
Si	2.3	0.1*	1.1	2.5	2.6	4.9	2.9	1.2	1.0	1.2	0.4	0.3	2.2	1.6	0.3*	0.4	1.1	3.6	0.5	0.8	0.6									
Sn	1.8	0.8	0.8	1.8	2.5	4.7	2.2	0.7	1.0	0.6	1.3	0.6	1.9	1.4	0.9	0.8	0.6	2.4	0.4	0.5	0.6	0.6								
Ta	2.7	0.2*	1.6	2.9	3.0	5.4**	3.5	1.6	1.3	1.7	0.4	0.6	2.6	2.0	0.4	0.3	1.6	4.2	0.8	1.2	0.9	0.2*	0.9							
Te	1.6	2.3	1.3	1.6	2.3	4.7	2.1	1.2	2.2	0.8	3.2	1.7	2.5	1.4	2.3	2.0	1.3	2.4	1.4	1.1	1.3	1.9	1.2	2.4						
Th	2.2	0.7	1.5	2.7	3.1	5.4**	3.4	1.7	1.7	1.4	1.0	0.9	2.8	1.8	0.5	0.6	1.6	4.1	1.0	1.2	0.8	0.4	1.1	0.5	2.0					
Ti	2.4	0.2*	1.1	2.5	2.9	5.0	2.7	1.0	0.7	1.1	0.6	0.2*	2.1	1.6	0.6	0.7	0.9	3.3	0.3*	0.9	0.7	0.3*	0.5	0.5	2.0	1.0				
U	1.3	1.8	1.2	1.4	2.4	5.4**	2.0	1.1	1.9	0.8	2.5	1.2	2.7	1.3	1.9	1.5	1.1	2.4	1.2	1.0	0.9	1.5	0.9	1.9	0.9	1.5	1.6			
V	2.2	1.3	1.0	2.4	3.0	4.6	2.5	0.6	1.0	0.3*	2.0	0.8	1.9	1.5	1.5	1.5	0.3	2.4	0.2*	0.7	0.8	1.1	0.6	1.6	1.4	1.6	0.7	1.3		
W	1.9	1.4	0.7	1.8	1.9	4.1	2.0	0.7	1.4	0.6	2.1	1.1	1.8	1.4	1.5	1.3	0.9	2.2	0.7	0.5	0.9	1.1	0.4	1.5	1.0	1.6	1.1	1.0	0.8	
Zr	2.6	0.1*	1.4	2.8	3.0	5.1**	3.2	1.4	1.2	1.5	0.3	0.5	2.4	1.8	0.4	0.4	1.3	3.8	0.6	1.1	0.8	0.1*	0.8	0.2*	2.2	0.6	0.3	1.8	1.3	1.4

The extended variation matrix is given in Appendix 2, Table A1; high and low values are highlighted as ** and *, respectively

Downloaded from http://pubs.geoscienceworld.org/segweb/economicgeology/article-pdf/117/4/853/5581376/4904_dmitrijeva_et_al.pdf
by China Geological Library user

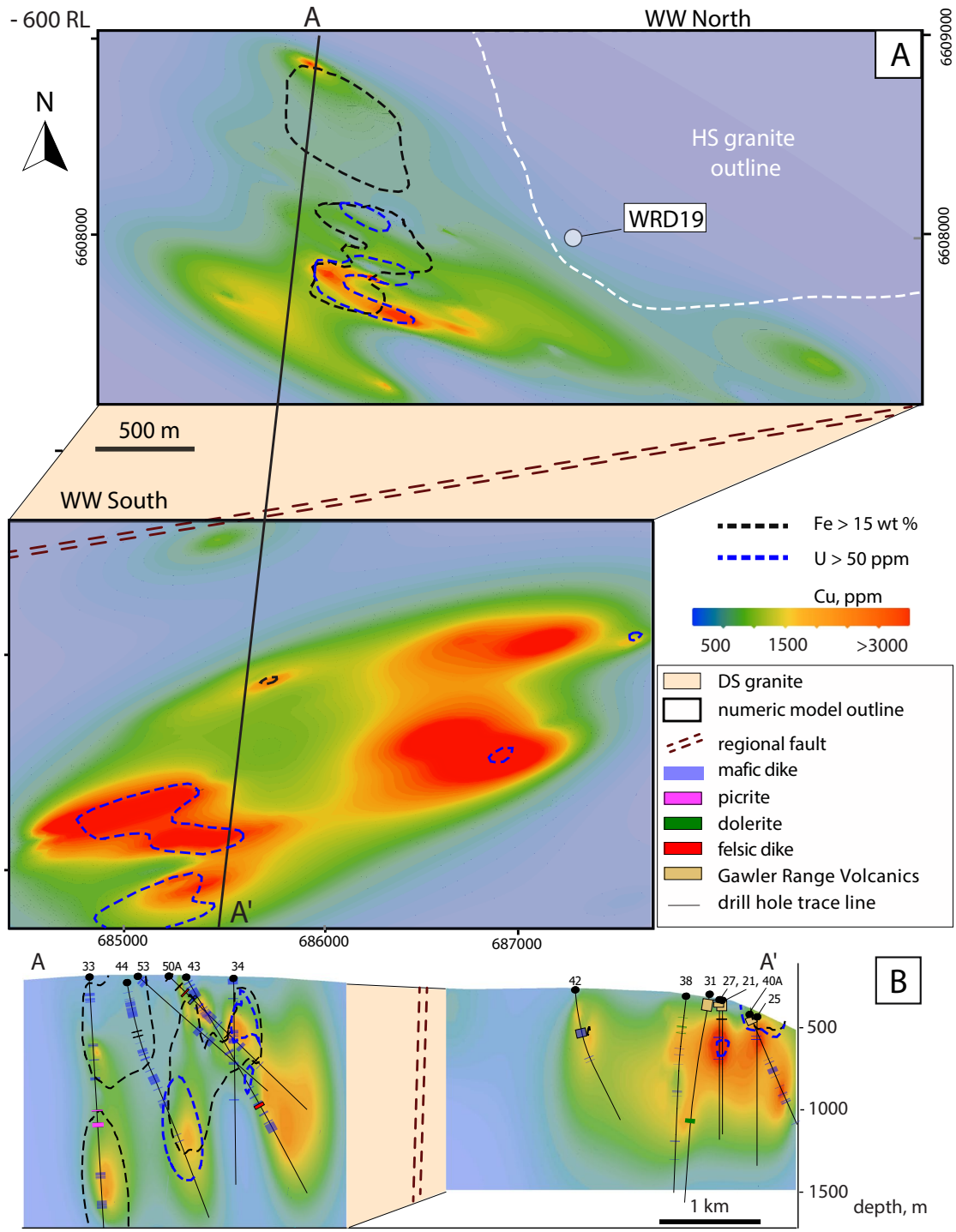

Fig. 6. Spatial distribution of Cu in WW-North and WW-South obtained via kriging, shown in plan view (A) and in cross section A-A' (B). Note that Fe anomalies are placed along the mafics, increasing with depth (>15 wt % Fe at >1,500 m) in WW-North, but shallower, broader, and weaker in WW-South. The U anomalies (>50 ppm) are located within or next to the Fe >15 wt % outline. The strongest U anomaly (~80 ppm) is located on the eastern side of WW-South. Note Cu anomalies (>500 ppm) along the mafics with wider and stronger concentrations (>3,000 ppm) in WW-South.

attributed to the "transition from magnetite to hematite," reflecting the change from magnetite- to hematite-dominant mineralization.

Group F ("hematite and Cu-Au mineralization") represents a distinct node on the dendrogram and includes the commodity metals (Cu, Au, U and Ag) together with trace elements that are closely associated with Cu(-Fe) sulfides (Bi and Te) or hematite (Mo).

Lithogeochemical clusters: Principal component analysis and k-means clustering: Principal component (PC) analy-

Downloaded from http://pubs.geoscienceworld.org/segweb/economicgeology/article-pdf/117/4/853/5581376/4904_dmitrijeva_et_al.pdf
by China Geological Library user

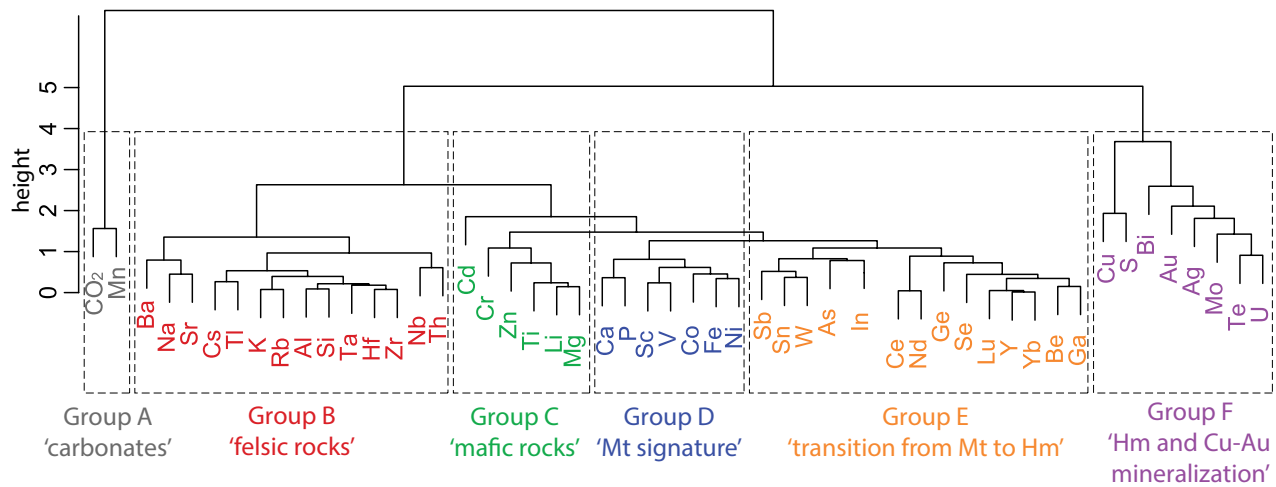

Fig. 7. (A) Hierarchical cluster dendrogram showing six geochemical groups (groups A-F) drawn from 51 analyzed elements. The height of each element on the dendrogram is a measure of dissimilarity calculated from the pairwise log-ratio matrix (Table 2; App. 2, Table A1) using Euclidean metrics.

sis results in PC loadings, which represent the associations among the groups of elements (a full list of element weightings on each PC is given in Table 3), and PC scores, where a score is assigned to each sample within the data. Insights into clusters and their petrological significance are provided by the PC1-PC2 and PC1-PC3 plots (Figs. 8 and 9) using a distinct color for picrite samples. Elements showing loadings ≥0.20, either positive or negative, for these three PCs are as follows:

PC1: –(0.34 × S; –0.29 × CO_2; –0.26 × Cu; –0.21 × Bi; –0.20 × Te) and (0.24 × K; 0.21 × Ba; 0.20 × Rb);

PC2: –(0.67 × CO_2; –0.40 × Mn) and (0.32 × Ag; 0.26 × Au; 0.22 × Cu);

PC3: –(0.49 × Bi; –0.28 × CO_2; –0.22 × Cu) and (0.30 × Ni; 0.29 × V; 0.21 × Cd).

The PC1-PC2 plot (Fig. 8A) shows three high-loading element associations with distinct orientation to one another. Significantly, the two associations in the upper part of the diagram with the highest loadings on PC2 have opposing directions on PC1 and comprise elements from the "felsic rocks" (group B) and the "hematite and Cu-Au mineralization" (group F). The other groups, C-E, have lower loadings and plot around the center of the diagram. Carbonates represented by elements in group A, with highest element loadings for CO_2 and Mn on both PC1 and PC2, form a third association in the lower part of the diagram, with opposite orientation (negative loadings on PC2) to the other two high-loading associations, thus indicating a geochemical signature that cannot be readily related to either the felsic rocks or hematite and Cu-Au mineralization.

Five lithogeochemical clusters (Table 4) are obtained by the k-means clustering method (App. 1) for all samples in the compiled data set (panels B-D in Figs. 8, 9). The score plots are projections of all data onto PC planes that maximize the proportion of the total variance within the data set. Each sample is strictly assigned to one of five geochemical clusters depicted at Wirrda Well (App. 1). The positions of the samples in proximity to each other on the score plots reflect their chemical similarity. The robustness of the scores is shown in the high values of Jaccard similarity coefficients (j_i = 0.72 to 0.9; Table 4; App. 1).

On one side of the PC1-PC2 diagram are three clusters corresponding to element groups defining felsic and mafic rocks, or a mixture thereof. Felsic "barren" lithologies (granites from Donington and Hiltaba suites) are defined by Cluster 4, on the right part of the diagram with high loadings of elements from felsic rocks (group B) such as Si, Al, K, Na, Ba, Rb, Hf, Ta, etc., while containing negligible Cu and Au (Table 4). Altered, undifferentiated mafic and felsic lithologies (granites and dolerite dikes) form two sizeable clusters (Cluster 1 above, and Cluster 2 below) in the central part of the diagram, attributed to mineralized and barren lithologies. Clusters 1 and 2 represent samples with "mixed" signatures and no characteristic group of elements that is uniquely associated with them. The "mineralized felsic and mafic rocks" in Cluster 1 can, however, be readily distinguished from the barren felsic rocks in Cluster 4 by the relatively high concentration of Cu and Au (Table 4). Samples representing the barren lithologies from Cluster 2 are characterized by a pronounced Mn-CO_2 (group A) signature, which is likely attributable to a combination of factors (e.g., derived from alteration of mafic rocks which are richer in CO_2 and/or multiple generations of siderite along shear zones; Courtney-Davies et al., 2019).

In contrast, the mineralization signatures are typified by two distinct clusters: Cluster 3 (defining a "hematite signature") and Cluster 5 ("magnetite signature") plotting on the left side of the diagram (Fig. 8B). Hematite- and magnetite-dominant samples are discriminated, even if there is a degree of overlap between them in the signatures of group E ("transitional from Mt to Hm"), which consists of elements found in both Fe oxides.

Samples from the two parts of the prospect, WW-North and -South, show a high degree of overlap on the PC1-PC2 plot (Fig. 8C), whereas the petrophysical properties (Fig. 8D) allow further characterization of clusters representing felsic lithologies (median ρ = 2.73 kg/m^3; median χ = 1.01 ×10^{-3}

Downloaded from http://pubs.geoscienceworld.org/segweb/economicgeology/article-pdf/117/4/853/5581376/4904_dmitrijeva_et_al.pdf
by China Geological Library user

Table 3. Results of Principal Component Analysis (PCA) Given as the Proportions of Explained Variance by First, Second, and Third Principal Components, with Loadings

Eigenvalues of PC1-PC3			
Eigenvalues	PC1	PC2	PC3
λ	3.36	2.45	1.84
λ%	29	15	8
$\Sigma\lambda$%	29	44	52
Loadings of the elements on PC1-PC3			
Elements	PC1	PC2	PC3
Ag	–0.14	**0.32**	–0.07
Al	0.15	–0.05	–0.08
As	–0.09	0.04	–0.01
Au	–0.16	**0.26**	–0.16
Ba	**0.21**	0.02	–0.06
Be	0.05	0.00	0.11
Bi	**–0.21**	0.15	**–0.49**
CO_2	**–0.29**	**–0.67**	**–0.28**
Ca	–0.04	–0.12	0.14
Cd	0.03	0.04	**0.21**
Ce	–0.03	0.09	–0.04
Cu	**–0.26**	**0.22**	**–0.22**
Co	–0.12	–0.01	0.16
Cs	0.19	0.00	–0.04
Cr	0.05	–0.01	0.10
Fe	–0.15	0.02	**0.20**
Ga	0.03	–0.03	0.09
Ge	–0.06	–0.03	0.12
Hf	0.18	–0.06	–0.12
In	–0.02	0.01	–0.13
K	**0.24**	–0.06	–0.09
Li	0.07	0.02	0.05
Lu	0.06	0.02	0.00
Mg	0.06	–0.02	0.08
Mn	–0.18	**–0.40**	–0.03
Mo	–0.11	0.16	–0.07
Na	0.16	0.00	–0.08
Nb	0.10	–0.01	–0.10
Nd	–0.02	0.07	–0.03
Ni	–0.09	–0.04	**0.30**
P	–0.04	–0.07	0.10
Rb	**0.20**	–0.05	–0.02
S	**–0.34**	–0.02	0.13
Sc	0.01	–0.04	0.16
Sb	–0.07	0.00	0.02
Se	0.00	0.03	0.06
Si	0.12	–0.04	–0.07
Sn	–0.03	0.02	0.08
Sr	0.16	0.05	–0.18
Ta	0.17	–0.04	–0.12
Te	**–0.20**	0.11	0.01
Th	0.11	0.02	–0.08
Ti	0.09	–0.04	0.06
Tl	0.19	–0.01	0.02
U	–0.13	0.17	0.04
V	–0.07	–0.03	**0.29**
W	–0.13	0.01	0.00
Y	0.06	0.02	–0.01
Yb	0.07	0.01	–0.01
Zn	0.08	0.07	0.19
Zr	0.15	–0.05	–0.08
LOI	–0.04	–0.11	–0.03

Notes: Numbers in bold indicate absolute loadings of the elements with ≥0.2; loadings are coordinates of the elements on the PCs projection; see Figures 8A and 9; LOI = lost on ignition

SI; Table 4) and mineralization. The latter are typified by the highest median densities and median magnetic susceptibilities for hematite and magnetite clusters, respectively. The "magnetite signature" cluster (median χ = 55 x 10^{-3} SI; Table 4) shows the highest proportion of Fe and V among all clusters and represents samples in which magnetite is the dominant Fe oxide. In contrast, the "hematite signature" cluster contains the highest concentrations of Cu and Au while still showing a relatively high proportion of Fe as well as magnetic susceptibility (Table 4).

The PC1-PC3 plots (Fig. 9) allow further insight into the geochemical signatures that better discriminate the defined lithogeochemical clusters, particularly allowing a clear-cut separation of the two mineralization signatures (Fig. 9A, B). The "hematite signature" (Cluster 3) is characterized by elements from group F (Hm and Cu-Au mineralization), with Bi, Cu, Au, Ag, and Mo, as well as U-W-Sn, As-Sb-Te, and light REEs showing the negative loadings on PC3. The "magnetite signature" (group D; Fe-Ni-Co-V-Sc-Ca-P) shows positive loadings on PC3 and an association with Cluster 5 attributed to the magnetite-dominant samples. The PC1-PC3 plots also discriminates granites from the Hiltaba and Donington suites (Fig. 9B), thus indicating significant primary magmatic geochemical differences between them.

The PC1-PC3 plot also highlights the significant geochemical differences between WW-North and WW-South and their distinct magnetic susceptibilities (Fig. 9C, D). The plot also shows the picrites (as identified from geologic logging) as a distinct subcluster with Zn-Cd-Cr (Zn ~1,000 ppm) as an element set typifying their geochemical signature.

Extrapolation of lithogeochemical clusters: Random Forest classification

Sample classification (App. 1) using the RF algorithm (Table 5) was applied to extrapolate the lithogeochemical clusters obtained from the compiled data set to the larger, limited elements data set (Fig. 10). This allows recognition of mineralization signatures in the remaining 38 drill holes not analyzed for trace elements of high exploration significance, such as As, Ag, Mo, REEs, and W. The classification model has an 88% accuracy rate based on the number of misclassified samples (Table 5).

Cluster 4, representing barren felsic lithologies, is the least misclassified, whereas the mineralization signatures (Clusters 3 and 5) are the most misclassified. The mean decrease in Gini index, a measure of the contribution of a given element to correctly classify data, was used to determine the relevance of different elements during classification (Fig. 10A). Copper, Mn, CO_2, Au, and Fe, as well as density and magnetic susceptibility, are among the most important variables facilitating this classification. PCA was applied to the limited element suite in order to check whether the predicted clusters show good correlation with the results of PCA on the compiled suite data set (Figs. 8A, B and 10B, C). This provides further validation of the RF classification method to data sets limited in analyzed elements.

The two clusters representing mineralization (Clusters 3 and 5) are the most important outcomes of the classification. Projection of mineralization clusters shows that WW-South and WW-North are dominated by the hematite and magnetite signatures, respectively (Fig. 10D, E). Moreover, the hematite signature (Cluster 3) matches the high-grade (>1,500 ppm Cu) shell, especially well developed in WW-South (Fig. 10D). The >15 wt % Fe outline shows a mismatch with the

Downloaded from http://pubs.geoscienceworld.org/segweb/economicgeology/article-pdf/117/4/853/5581376/4904_dmitrijeva_et_al.pdf
by China Geological Library user

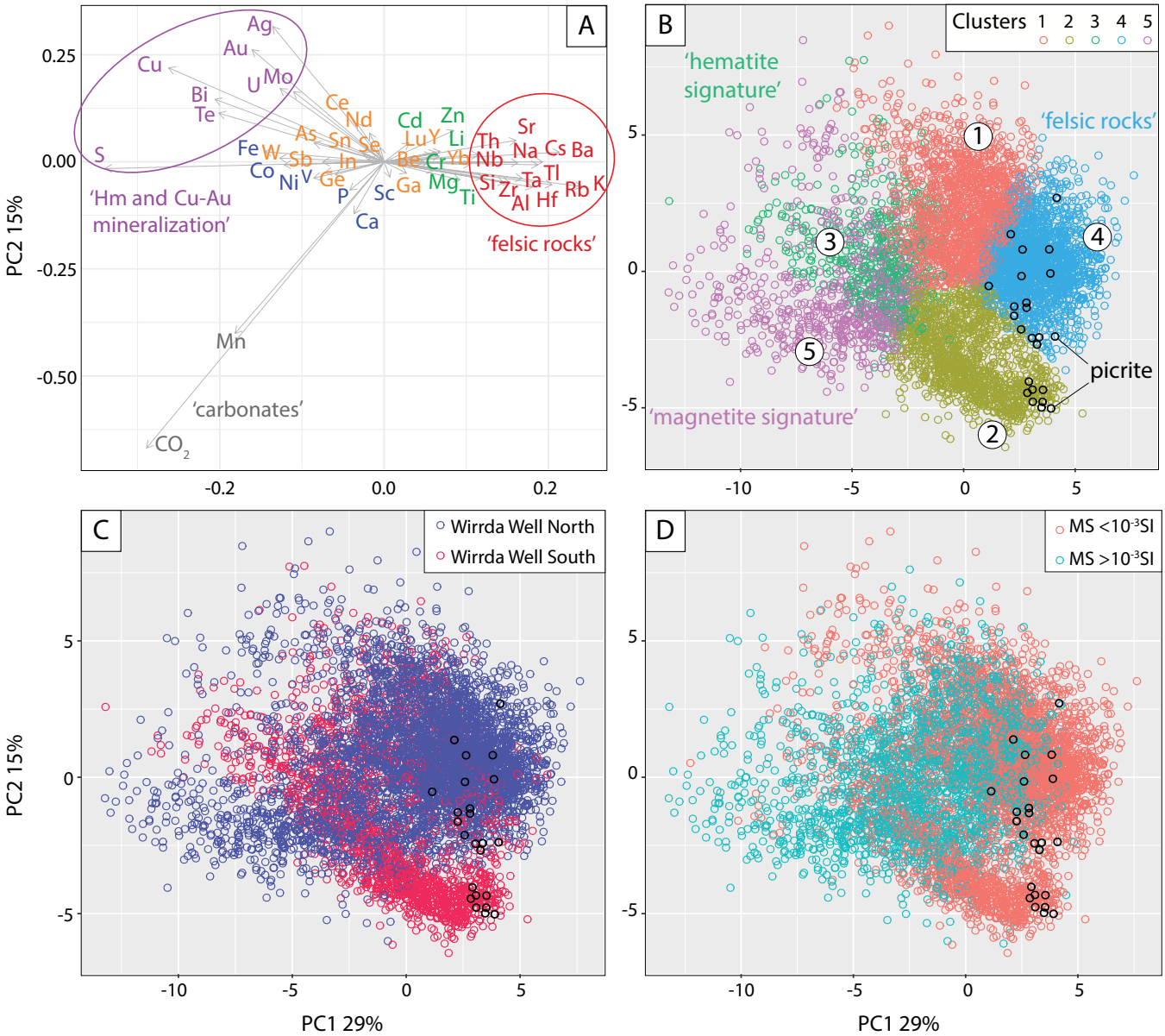

Fig. 8. Projection of PC1 vs. PC2 showing (A) principal component loadings (color-coded according to the hierarchical dendrogram in Fig. 6) obtained from the centered log-ratio–transformed compiled suite data. (B) Distribution of Clusters 1 through 5 (color-coded and numbered) according to principal component scores. Each point (circle) represents a single sample. (C) The same data separated into samples from WW-North and -South. (D) The same data split into the two magnetic susceptibility (MS) categories.

>1,500 ppm Cu shell, especially in WW-South. In contrast, the "magnetite signature" cluster (Cluster 5), representing elevated Fe-V-Ni-Co and low Cu-Au contents, is weakly developed in WW-South but is dominant in WW-North. This is also shown by the significant overlap between the "magnetite" cluster and samples >15 wt % Fe shell (Fig. 10E).

Geochemical trends defining IOCG alteration

Geochemical trends representative of IOCG alteration were tested for the five lithogeochemical clusters using the limited element data set (29,172 whole-rock analyses), color-coded and numbered according to cluster membership predicted by RF classification. Meaningful trends are obtained when plotting Na/Al (sodic) and K/Al (K-feldspar to sericite) ratios against a Fe-Mg-Mn-Ca index depicting elements representing chlorite, Fe oxides, and carbonates (Fig. 11). Calcium was included in this index, as it can be considered a proxy for relict calcic plagioclase in the lithologies, as well as for fluorapatite coexisting with magnetite.

Clusters representing lithologies show an overlap with respect to sodic alteration, whereby the Hiltaba Suite granite plots closer to stoichiometric albite (Fig. 11A). On the same plot, the mixed lithologies, altered and mineralized (Clusters 1 and 2), show greater degrees of Fe oxide + carbonate alteration than the barren felsic lithologies (Cluster 4). The magnetite cluster (Cluster 5) shows the strongest spread, defining a trend

Downloaded from http://pubs.geoscienceworld.org/segweb/economicgeology/article-pdf/117/4/853/5581376/4904_dmitrijeva_et_al.pdf
by China Geological Library user

Table 4. Characteristics of Five Clusters Obtained from *k*-means Cluster Analysis Applied to Compiled Suite Data

Cluster no (#)	Lithogeochemical signature	No. of samples (*N*)	Jaccard similarity value (j_i)	Silhouette value	Median Cu (ppm)	Median Au (ppb)	Median density (kg/m³)	Median magnetic susceptibility (×10⁻³ SI)
Altered, mixed felsic and mafic rocks (DSG and dolerite dikes)								
1	Mineralized	1,566	0.77	0.11	2,600	60	2.98	4.23
2	Less mineralized	1,319	0.90	0.31	500	11	2.81	2.12
4	Barren felsic rocks (DS and HS granites)	1,891	0.85	0.25	250	13	2.73	1.01
Mineralization								
3	Hematite	733	0.72	0.28	7,150	100	3.12	9.25
5	Magnetite	646	0.81	0.16	150	10	3.82	55.18

Notes: = number of whole-rock samples within each cluster; calculated cluster stability and silhouette values are from Appendix 1, Figure A3; median densities and median values of Fe, K are in in wt %

Abbreviations: DS = Donington Suite; DG = Donington Suite granites; HS = Hiltaba Suite

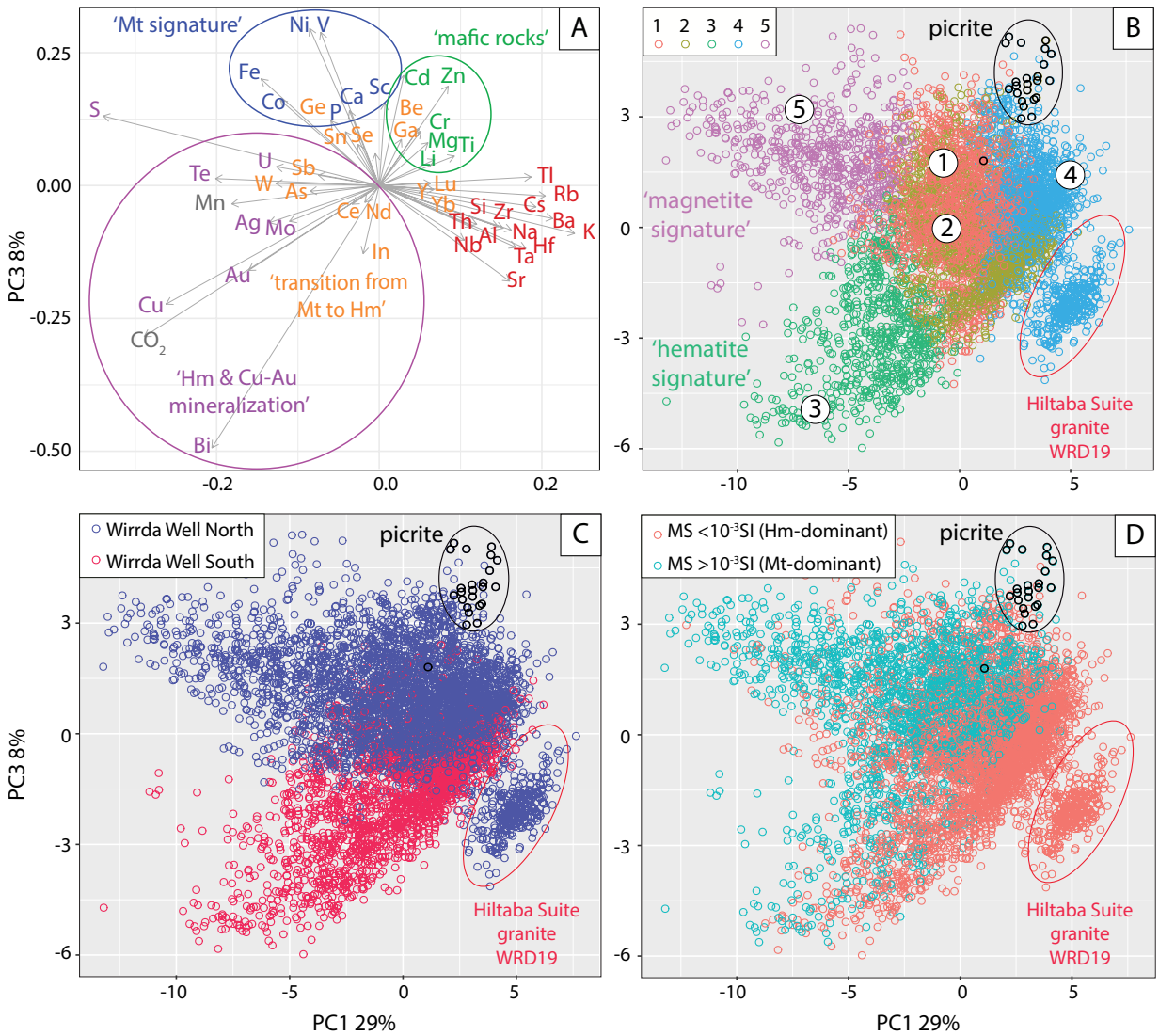

Fig. 9. Projection of PC1 vs. PC3 showing (A) principal component loadings (color-coded according to the hierarchical dendrogram in Fig. 6). (B) Distribution of Clusters 1 through 5 (color-coded and numbered) according to principal component scores. Each point (circle) represents a single sample. (C) The same data separated into samples from WW-North and -South. Note high loadings of group C (mafic rocks) elements for picrite samples and clustering of samples from the Hiltaba granite drill hole (WRD19) apart from other sample groups. (D) The same data split into the two magnetic susceptibility (MS) categories.

Downloaded from http://pubs.geoscienceworld.org/segweb/economicgeology/article-pdf/117/4/853/5581376/4904_dmitrijeva_et_al.pdf
by China Geological Library user

Table 5. Confusion Matrix of the Random Forest (RF) Classification of Five-Level Response Variable "Cluster" Onto Bootstrapped Test Sample (n = 21,264)

Cluster	1	2	3	4	5
1	5,833	87	49	270	81
2	159	5,010	131	179	17
3	157	78	958	0	26
4	562	244	1	11,137	0
5	87	56	47	0	1,095
n, total	6,798	5,475	1,186	11,586	1,219
n, misclassified	965	465	228	449	124
Percentage misclassified, %	14.1	8.5	19.2	3.9	10.2
Model accuracy, %	88				

Notes: True classes are arranged by columns; predicted classes are within rows

combining albitization and Fe metasomatism, whereas the hematite cluster (Cluster 3) shows neither, but instead occupies the same position as the altered/mineralized lithologies (Clusters 1 and 2) in terms of Fe oxide + carbonate alteration, plotting below magnetite but above the felsic lithologies (Fig. 11B).

The clusters representing the lithologies plot as an extended array in terms of sericitic alteration. Hiltaba Suite granite and GRV plot closest to stoichiometric K-feldspar and sericite, respectively (Fig. 11C). The mixed altered and mineralized lithologies overlap with one another on the same diagram and show chloritization. The hematite cluster shows a spread for sericitic alteration comparable to that of the felsic lithologies, whereas the magnetite cluster shows a marked chloritic alteration (Fig. 11D). The hematite cluster occupies a similar position on the index axis as the mixed altered + mineralized lithologies, whereas the magnetite cluster plots above, indicating that these rocks display the greatest degree of Fe + carbonate alteration (Fig. 11D).

Discussion

Lithological and structural controls on the mineralization at Wirrda Well

The downhole distribution pattern of mafics predating mineralization is markedly different in WW-North and WW-South (Figs. 3B, 6B). The Fe distribution shows good correlation with the samples logged as undifferentiated dikes, albeit lithological control is markedly stronger in WW-North than -South, in agreement with the exploration model (compare Fig. 2B-C with Fig. 6B), suggesting that dike-granite contacts serve as fluid conduits.

The WW-North and WW-South can be considered as two distinct, small-scale structural blocks that were either already separated from one another or became separated after pre-Hiltaba dike emplacement. Block rotation during the SLIP extensional regime (marked by arrows on Fig. 2A; Hayward and Skirrow, 2010) can be suggested to match the relationships between the two WW blocks. Wirrda Well, unlike other prospect/deposits in the area, displays two important characteristics which, if understood in genetic terms, could (1) resolve the role of mafic lithologies/dikes in providing metal sources (assumed by some authors, e.g., Haynes et al., 1995 and Huang et al., 2016) and (2) establish the significance of magnetite- and hematite-dominant domains at comparable depths, yet in distinct structural blocks, as we suggest here (Figs. 3A, 6). If we assume the two domains were the deeper and shallower levels of a single IOCG system that evolved in time, WW-South would represent a down-dropped block relative to WW-North. A comparable situation, albeit one in which the magnetite-dominant block is barren, is known from Prominent Hill, an IOCG deposit ~170 km northwest of Wirrda Well (Freeman and Tomkinson, 2010). Alternatively, the two WW domains discussed here could represent distinct IOCG systems, in turn implying that the upper part of WW-North was eroded, whereas the root of WW-South is still below the level of drill hole exposure. Constraining either of the two alternatives requires dedicated structural-geochronological studies. Doing so could, however, generate outcomes enabling an optimization of exploration strategies for IOCG mineralization in the Gawler Craton and elsewhere.

The statistical analysis shows that alteration accompanied by different degrees of Cu-Au mineralization is represented in a majority of data forming the mixed felsic and mafic lithologies (Clusters 1 and 2; Figs. 7B, 8B, 9B; Table 4), suggesting that both the host Donington granite and undifferentiated mafic dikes were brecciated and altered by fluids postdating their emplacement. This highlights the fact that the mineralization is centered in granite/dike contacts, suggesting a structural control for focusing of fluids and metal traps from underneath such structures with breccias propagating into both lithologies. Analogous granite-mafic lithological contacts in cratonic terranes are host to many orogenic Au deposits worldwide (e.g., Goldfarb et al., 2001).

Wirrda Well can thus be considered a lithologically and structurally controlled mineral deposit whereby lithological contacts, faults, and their impact on metal zonation patterns are more prominent than at Olympic Dam.

Significance of multivariate statistical analysis: IOCG signatures of the Olympic Dam district

Wirrda Well is one of the prospects in which multistage alteration (pre-, syn-, and post-IOCG event) has affected the primary lithologies, making it challenging to discriminate geochemical signatures of Fe oxides associated with Cu-Au-U mineralization by simple statistical methods. Multivariate statistical analysis provides a tool to process the large, whole-rock geochemical data sets necessary to discriminate lithologies with comparable alteration and constrain the specific signatures for Fe oxide mineralization.

The results here show that lithogeochemical clusters, defining primary lithologies and alteration assemblages that share comparable geochemistry (Table 4), can be discriminated by two different statistical methods, k-means clustering and PCA (Figs. 8–10). The good match between the two methods is proof of the robustness of the approach. Although the geochemical signatures associated with Cu-Au-U mineralization are biased by carbonate alteration expressing the highest loadings/scores on PC1-PC2 diagrams (Fig. 8), the mineralization signatures become apparent among the second order elements defining the PCI-PC3 plots (Fig. 9). Such analysis complements the simpler approach defining geochemical groups of elements using dendrograms or variation matrices (Fig. 7).

Downloaded from http://pubs.geoscienceworld.org/segweb/economicgeology/article-pdf/117/4/853/5581376/4904_dmitrijeva_et_al.pdf
by China Geological Library user

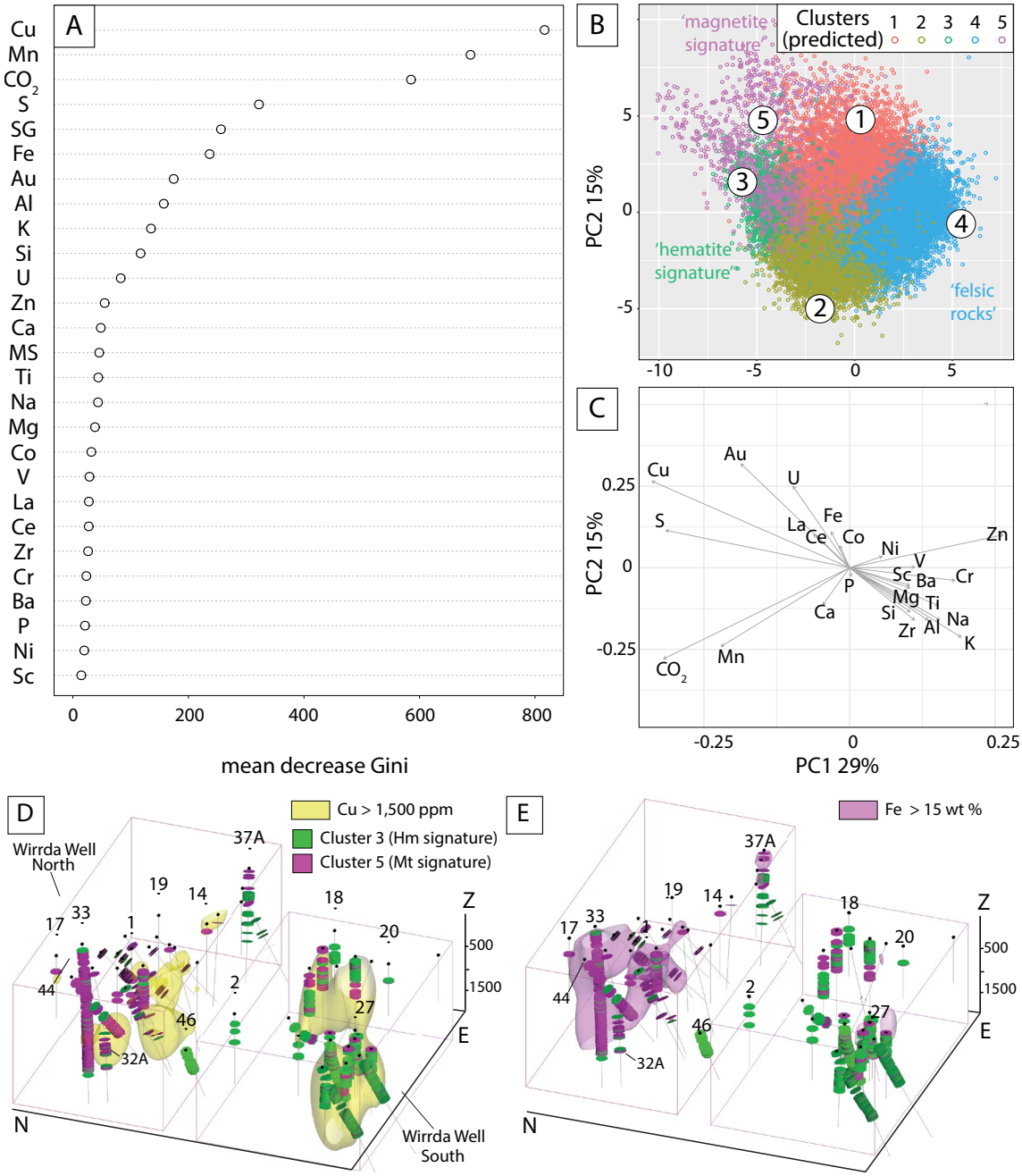

Fig. 10. (A) Diagram showing variable importance as "mean decrease Gini index" obtained from Random Forest (RF) model classification. The 28 predictors are ordered according to their contribution into correct classification of the training data. Copper, Fe, Au, and specific gravity (SG) are among the most important for the classification, whereas Ni and Sc are the least important. (B) Principal component scores and (C) loadings obtained from principal component analysis (PCA) of the limited suite data. Each sample (circle) is color-coded according to the predicted cluster from the RF model. (D, E) Oblique view (plunge 30°; azimuth 70°) of WW-North and -South showing isosurfaces of Cu >1,500 ppm (D) and Fe >15 wt % (E) overlain by geochemical clusters relevant for the "hematite" (Hm) (Cluster 3) and "magnetite" (Mt) signatures (Cluster 5). Note the spatial correlation between the "hematite" signature (Cluster 3) and Cu distribution in WW-South. Abbreviation: MS = magnetic susceptibility.

The clear geochemical discrimination between magnetite and hematite, which appear as separate clusters (Clusters 3 and 5 on Fig. 9B), is a valuable result for identifying IOCG signatures, since this type of breccia-hosted mineralization can be highly irregular or patchy throughout a given deposit. Considering the lithologies at Wirrda Well, alteration trends highlighted in the present study are albitization, Fe(Ca) alteration, sericitization, chloritization, and a generic "carbonate" alteration (Fig. 11A-D). Among these, the chlorite and carbonate alterations, affecting both Donington Suite gran-

Downloaded from http://pubs.geoscienceworld.org/segweb/economicgeology/article-pdf/117/4/853/5581376/4904_dmitrijeva_et_al.pdf
by China Geological Library user

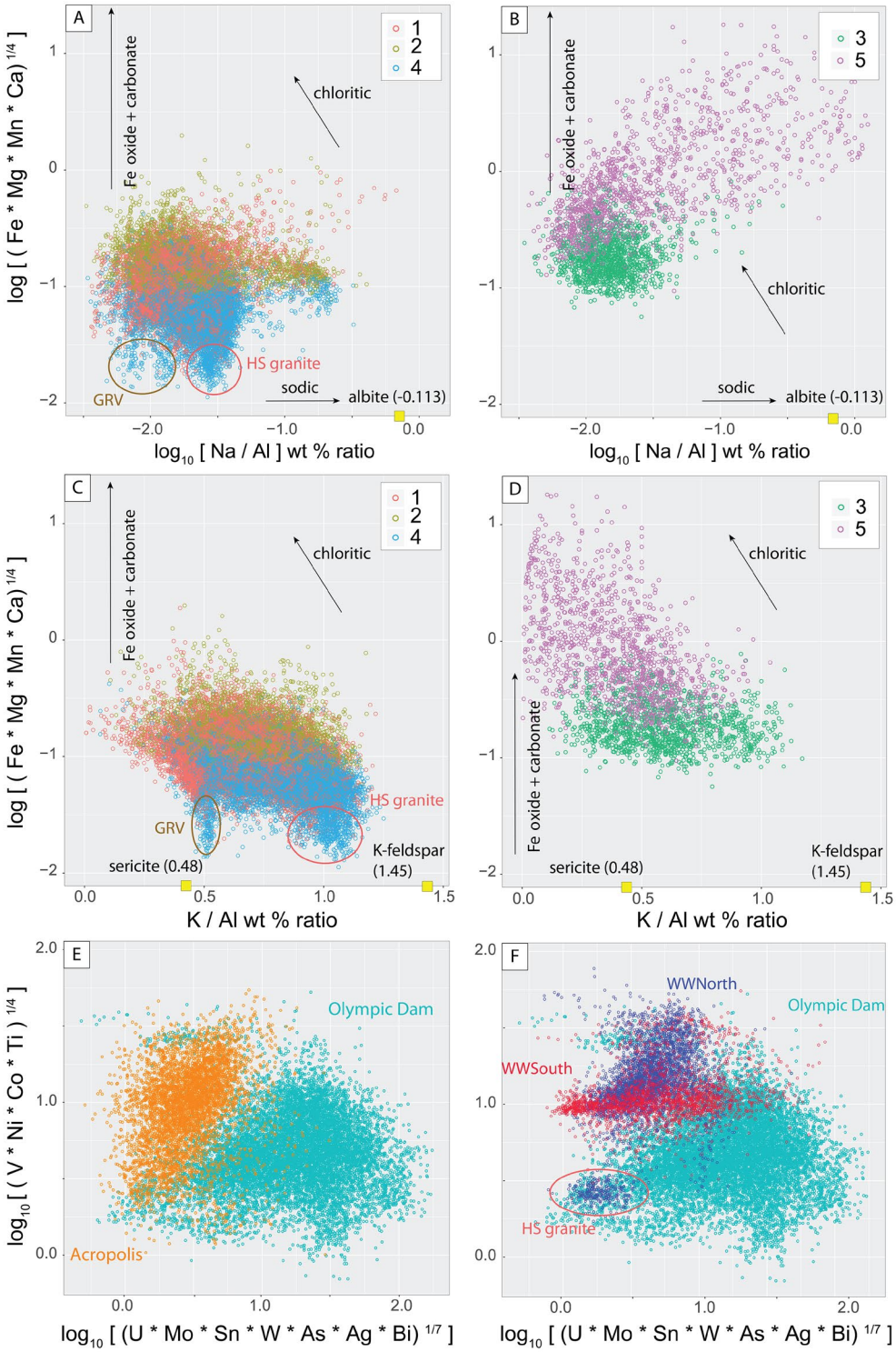

Fig. 11. (A-D) Geochemical trends representative of iron oxide copper-gold (IOCG) alteration (as marked) plotted for the five lithogeochemical clusters using the limited element data set (29,172 whole-rock analyses), color-coded and numbered according to cluster membership predicted by Random Forest (RF) classification. (A, B) Sodic alteration represented by increase in Na/Al is depicted by the Hiltaba Suite granite and the magnetite cluster (Cluster 5). (C, D) K-feldspar to sericite transition is less dominant in Hiltaba Suite granite but is near ubiquitous in the remaining samples, and particularly in the hematite cluster (Cluster 3). Chlorite + carbonate + Fe alteration is depicted by the mixed felsic and mafic lithologies (Clusters 1 and 2; A and C) and by the magnetite cluster (D). (E, F) Plots of all samples in terms of "granitophile" + chalcophile elements vs. transitional metals, considered as key elements for comparison of IOCG signatures in the Olympic Dam district. Data for Olympic Dam and Acropolis from Dmitrijeva et al. (2019a, b). WW-North (magnetite-dominant) and Acropolis are higher in transitional metals and overlap with one other. In contrast, WW-South (hematite-dominant) partially overlaps with Olympic Dam.

Downloaded from http://pubs.geoscienceworld.org/segweb/economicgeology/article-pdf/117/4/853/5581376/4904_dmitrijeva_et_al.pdf
by China Geological Library user

ite and the undifferentiated dikes, could have formed during episodes of fault/shear zone reactivation events that both pre- and postdate the ~1.6 Ga IOCG event.

In geochemical terms, alkali alteration, both sodic and potassic, is associated with increased Fe metasomatism (magnetite-dominant), typical of IOCG systems. Such alteration is difficult to evaluate for deposits hosted by granitoids, particularly if changes in mineralogy are not due to input of Na and K from external fluids but rather the result of rock-buffered fluid-mineral reactions (metasomatism) leading to formation of new albite and K-feldspar without substantial changes in whole-rock geochemistry. This type of mineralogical alteration is essentially isochemical and has been documented in petrological-geochemical studies of granitoids in the Olympic Dam district, including at Wirrda Well (Mauger et al., 2016; Kontonikas-Charos et al., 2017, 2018). Alteration of igneous feldspar results in sericite + hematite ± calcite assemblages (Kontonikas-Charos et al., 2017), developing into a distinct, hydrolytic (sericite + hematite) alteration in granite-derived breccias hosting Cu-Au mineralization, as documented from the Olympic Dam deposit (Ehrig et al., 2012). Sericitic alteration of host Hiltaba Suite granite is clearly revealed by statistical analysis of whole-rock data from Olympic Dam (Dmitrijeva et al., 2019a). At Wirrda Well, sericitic alteration is present in the barren felsic lithologies and hematite clusters (Clusters 4 and 3, respectively; Fig. 11C, D). Such results are comparable with patterns obtained for the comparable felsic lithologies from the Acropolis prospect (Dmitrijeva et al., 2019b).

Collectively, these selected alteration diagrams show that in Wirrda Well, sodic (+ calcic) alteration is associated with magnetite formation, an early, sulfide poor/barren stage, whereas hydrolytic alteration (sericite formation) is associated with hematite, the sulfide-richer stage of some IOCG systems (Barton, 2014, and references therein).

The geochemical signatures obtained for lithogeochemical clusters representing Fe oxides are instructive for comparing the three IOCG systems in the Olympic Dam district studied using comparable statistical approaches (Table 6). The hematite signature from Wirrda Well incorporates Cu-Au-U and shows a common enrichment in W-Sn-Mo (granitophile elements), chalcophile elements (Bi-Ag-As-Sb-Te) and light (L)REEs with Olympic Dam (Dmitrijeva et al., 2019a). At Acropolis, however, and despite the smaller data set, the hematite carries only U and a few other metals (Sn, Sb, and W), whereas Cu, Mo, and Bi are part of the magnetite signature (Table 6; Dmitrijeva et al., 2019b). The magnetite signatures from Wirrda Well and Acropolis share transitional group elements (Fe, V, Co, and Ni).

Such similarities and differences among the three IOCG systems in the Olympic Dam district are also apparent if all samples are plotted in terms of "granitophile" + chalcophile elements versus transitional metals (Fig. 11E, F). This shows that WW-North (magnetite-dominant) and Acropolis are higher in transitional metals and overlap with one other. In contrast, WW-South (hematite-dominant) partially overlaps with Olympic Dam.

Conclusions and Implications

The key conclusions from this study are as follows:

1. The Wirrda Well prospect contains two distinct spatial domains with IOCG-style mineralization: WW-North; and WW-South. These display geochemical differences including a "magnetite" signature in WW-North and a Mo-W-U(± Sn) "hematite" signature associated with higher-grade Cu-Au-(± Bi-Ag) mineralization in WW-South.
2. The contacts between host granite and premineralization mafic dikes emplaced along Early Proterozoic structures provide permeable structures for fluid focusing and metal deposition since Fe, Cu, and U are concentrated along such contacts; this is highlighted by lithogeochemical clusters representing both lithologies.
3. Although the geologic setting, mineralogy, and geochemistry of the Wirrda Well prospect show some dissimilarities with both Olympic Dam and Acropolis, there are nevertheless sufficient geochemical similarities to confirm a comparable source for hydrothermal fluids and metals.

This case study demonstrates how a combination of supervised and unsupervised algorithms for generation of geochemical clusters can efficiently characterize an orebody and its alteration and define the geochemical signatures of mineralization. The supervised RF algorithm applied to the limited

Table 6. Geochemical Signatures of Mineralization in the Olympic Dam Deposit and the Acropolis and Wirrda Well Prospects

Mineralization signature	Olympic Dam	Wirrda Well	Acropolis
Hematite		Dominant	
"Granitophile"(U-W-Sn-Mo) and chalcophile elements, LREEs	W-Mo-Au-As-Sb	Cu-Au-Bi (WW-South)	W-Sn-Sb
		Subordinate	
	U-Sn-Cu-Ag-Bi-Te-LREEs-Ca-P-Sr	Mo-W-U-Sn-Ag-Te-As-Sb-LREEs (WW-South)	U-LREEs-Th-Ca-P-Sr
Magnetite		Dominant	
Transition group elements	n.a.	Fe-V-Ni-Co (WW-North)	Fe-V-Ni-Co
		Subordinate	
		Ca-P-Sc (WW-North)	Cu-Bi-Mo

Notes: Data from the current study and Dmitrijeva et al. (2019a, b); a dominant signature represents elements with the strongest loading onto a PC1 obtained from a particular iron oxide copper-gold (IOCG) system; a subordinate signature corresponds to elements that have significant, albeit not dominant loadings onto the corresponding PC1; LREEs = light rare earth elements, n.a. = not analyzed – lies outside of the orebody

Downloaded from http://pubs.geoscienceworld.org/segweb/economicgeology/article-pdf/117/4/853/5581376/4904_dmitrijeva_et_al.pdf
by China Geological Library user

element suite data yields valid predictions when extrapolating the lithogeochemical clusters, thus it is a reliable and cost-effective tool for ore deposit characterization. The efficacy of RF is especially relevant as those elements that are characteristic of IOCG mineralization in the Gawler Craton (e.g., W, Mo, Sn, Bi, As, Sb, and Ag) were absent in the limited element suite data. On this basis, the combined approach represents an example of efficient orebody characterization and can be used for brownfields exploration around IOCG deposits and, potentially, for regional-scale exploration. Numeric interpolation of elements, when combined with advanced statistical analyses of geochemical data, can facilitate understanding of ore genesis in time and space.

The present statistical approach is different from other geochemical studies of whole-rock data using multivariate statistics or mineral alteration diagrams based on molar ratio vectors to support models of hydrothermal alteration in IOCG systems (e.g., in the Great Bear magmatic zone, Canada; Montreuil et al., 2013, and references therein). Studies of IOCG systems using the statistical approach we have used here may show whether the "Fe oxide signatures" represent an easier, more efficient way to compare deposits from different metallogenetic terranes. It would also be valuable to extend the approach and examine how IOCG and porphyry-style deposits compare with one another, since they share not only alkali alteration but also present-day economic commodities (Cu, Au, Mo), as well as enrichment in certain critical metals (Co, LREEs) for potential future recovery.

Acknowledgments

This work is a contribution to the FOX project "Trace elements in iron-oxides: Deportment, distribution and application in ore genesis, geochronology, exploration and mineral processing," supported by BHP Olympic Dam and the South Australian Mining and Petroleum Services Centre of Excellence. K.E. and M.C. acknowledge the Wirrda Well exploration team, who designed, drilled, and logged the Wirrda Well drill core. Maya Kamenetsky (Centre for Ore Deposit and Earth Sciences [CODES], University of Tasmania) kindly provided her unpublished zircon ages from WRD19. V.K. and J.M. acknowledge funding from the ARC Linkage Grant, "The supergiant Olympic Dam U-Cu-Au-REE ore deposit: towards a new genetic model." N.J.C. acknowledges additional support from the Australian Research Council (ARC) Research Hub for Australian Copper-Uranium (Grant IH130200033). The Leapfrog Geo support team is also kindly thanked for their assistance with the development of the geologic model. The authors thank Ayesha Ahmed, an anonymous reviewer, and the *Economic Geology* Editorial Board for valuable comments that help improve our original presentation of this work.

REFERENCES

Allen, S., McPhie, J., Ferris, G., and Simpson, C., 2008, Evolution and architecture of a large felsic igneous province in western Laurentia: The 1.6 Ga Gawler Range Volcanics, South Australia: Journal of Volcanology and Geothermal Research, v. 172, p. 132–147.

Barton, M.D., 2014, Iron oxide (-Cu-Au-REE-P-Ag-U-Co) systems, *in* Holland, H.D., and Turekian, K.K., eds., Treatise on Geochemistry, 2nd ed.: Elsevier, Oxford, p. 515–541.

Bérubé, C.L., Olivo, G.R., Chouteau, M., Perrouty, S., Shamsipour, P., Enkin, R.J., Morris, W.A., Feltrin, L., and Thiémonge, R., 2018, Predicting rock type and detecting hydrothermal alteration using machine learning and petrophysical properties of the Canadian Malartic ore and host rocks, Pontiac Subprovince, Québec, Canada: Ore Geology Reviews, v. 96, p. 130–145.

Betts, P.O., and Giles, D., 2006, The 1800–1100 Ma tectonic evolution of Australia: Precambrian Research, v. 144, p. 92–125.

Blissett, A.H., Creaser, R.A., Daly, S.J., Flint, R.B., and Parker, A.J., 1993, Gawler Range Volcanics: Geological Survey of South Australia, Bulletin 54, p. 107–131.

Breiman, L., 2001, Random forests: Machine Learning, v. 45, p. 5–32.

Caté, A., Schetselaarb, E., Mercier-Langevin, P., and Ross, P.-S., 2018, Classification of lithostratigraphic and alteration units from drillhole lithogeochemical data using machine learning: A case study from the Lalor volcanogenic massive sulphide deposit, Snow Lake, Manitoba, Canada: Journal of Geochemical Exploration, v. 188, p. 216–228.

Cherry, A.R., Kamenetsky, V.S., McPhie, J., Thompson, J.M., Ehrig, K.J., Meffre, S., Kamenetsky, M.B., and Krneta, S., 2018, Tectonothermal events in the Olympic IOCG Province constrained by apatite and REE-phosphate geochronology: Australian Journal of Earth Sciences, v. 65, p. 643–659.

Ciobanu, C.L., Wade, B.P., Cook, N.J., Schmidt Mumm, A., and Giles, D., 2013, Uranium-bearing hematite from the Olympic Dam Cu-U-Au deposit, South Australia; a geochemical tracer and reconnaissance Pb-Pb geochronometer: Precambrian Research, v. 238, p. 129–147.

Ciobanu, C.L., Slattery, A., Verdugo-Ihl, M., Courtney-Davies, L., Cook, N.J., and Ehrig, K., 2018, Crystal structural modifications in U-rich, oscillatory-zoned hematite [abs.]: Geochemical Society and European Association of Geochemistry, Goldschmidt, Boston, Massachusetts, 2018, Proceedings, p. 437.

Conor, C.H.H., Raymond, O., Baker, T., Teale, G., Say, P., and Lowe, G., 2010, Alteration and mineralization in the Moonta-Wallaroo copper-gold mining field region, Olympic Domain, South Australia, *in* Porter, T.M., ed., Hydrothermal iron oxide copper-gold and related deposits: A Global Perspective, v. 3: Porter GeoConsultancy Publishing, Adelaide, p. 147–170.

Corriveau, L., Montreuil, J.F., and Potter, E., 2016, Alteration facies linkages among iron oxide copper-gold, iron oxide-apatite, and affiliated deposits in the Great Bear Magmatic Zone, Northwest Territories, Canada: Economic Geology, v. 111, p. 2045–2072.

Courtney-Davies, L., Ciobanu, C., Verdugo-Ihl, M.R., Dmitrijeva, M., Cook, N., Ehrig, K., and Wade, B., 2019, Hematite geochemistry and geochronology resolve genetic and temporal links among iron-oxide copper gold systems, Olympic Dam district, South Australia: Precambrian Research, v. 335, article 105480.

Courtney-Davies, L., Ciobanu, C.L., Verdugo-Ihl, M.R., Cook, N.J., Ehrig, K.J., Wade, B.P., Zhu, Z.-Y., and Kamenetsky, V.S., 2020a, ~1760 Ma magnetite-bearing protoliths in the Olympic Dam deposit, South Australia: Implications for ore genesis and regional metallogeny: Ore Geology Reviews, v. 118, article 103337.

Courtney-Davies, L., Ciobanu, C.L., Tapster, S.R., Cook, N.J., Ehrig, K.J., Crowley, J.L., Verdugo-Ihl, M.R., Wade, B.P., and Condon, D.J., 2020b, Opening the magmatic-hydrothermal window: High-precision U-Pb geochronology of the Mesoproterozoic Olympic Dam Cu-U-Au-Ag deposit, South Australia: Economic Geology, v. 115, p. 1855–1870.

Creaser, R.A., 1989, The geology and petrology of Middle Proterozoic felsic magmatism of the Stuart Shelf, South Australia: Ph.D. thesis, Melbourne, Australia, La Trobe University, 434 p.

Cross, K., 1993, Acropolis and Wirrda Well prospects: Geological Survey of South Australia, Bulletin 54, p. 138.

Dmitrijeva, M., Ehrig, K.J., Ciobanu, C.L., Cook, N.J., Verdugo-Ihl, M.R., and Metcalfe, A.V., 2019a, Defining IOCG signatures through compositional data analysis: A case study of lithogeochemical zoning from the Olympic Dam deposit, South Australia: Ore Geology Reviews, v. 105, p. 86–101.

Dmitrijeva, M., Ciobanu, C.L., Ehrig, K.J., Cook, N.J., Metcalfe, A.V., Verdugo-Ihl, M.R., and McPhie, J., 2019b, Mineralization-alteration footprints in the Olympic Dam IOCG district South Australia: The Acropolis prospect: Journal of Geochemical Exploration, v. 205, article 106333.

Dmitrijeva, M., Cook, N.J., Ehrig, K., Ciobanu, C.L., Metcalfe, A.V., Kamenetsky, M., Kamenetsky, V.S., and Gilbert, S.E., 2020, Multivariate statistical analysis of trace elements in pyrite: Prediction, bias and artefacts in defining mineral signatures: Minerals, v. 10, 22 p..

Ehrig, K., 2013, Geology of the Wirrda Well IOCG deposit: South Australian Exploration and Mining Conference, 10th, Adelaide, 2013, Proceedings, PowerPoint presentation, http://saemc.com.au/archive/2013/13ehrig.pdf.

Downloaded from http://pubs.geoscienceworld.org/segweb/economicgeology/article-pdf/117/4/853/5581376/4904_dmitrijeva_et_al.pdf
by China Geological Library user

Ehrig, K., McPhie, J., and Kamenetsky, V., 2012, Geology and mineralogical zonation of the Olympic Dam iron oxide Cu-U-Au-Ag deposit, South Australia: Society of Economic Geologists, Special Publication no. 16, p. 237–267.

Ehrig, K., Kamenetsky, V.S., McPhie, J., Apukhtina, O., Ciobanu, C., Cook, N., Kontonikas-Charos, A., and Krneta, S., 2017, The IOCG-IOA Olympic Dam Cu-U-Au-Ag deposit and nearby prospects, South Australia: Society for Geology Applied to Mineral Deposits, Biennial Meeting, 14th, Québec City, Canada, 2017, Proceedings, p. 823–826.

Freeman, H., and Tomkinson, M., 2010, Geological setting of iron oxide related mineralisation in the Southern Mount Woods Domain, South Australia, *in* Porter, T.M., ed., Hydrothermal iron oxide copper-gold and related deposits: A global perspective, v. 3–4: Porter GeoConsultancy Publishing, Adelaide, p. 171–190.

Goldfarb, R.J., Groves, D.I., and Gardoll, S., 2001, Orogenic gold and geologic time: A global synthesis: Ore Geology Reviews, v. 18, p. 1–75.

Gregory, D.D., Cracknell, M.J., Large, R.R., McGoldrick, P., Kuhn, S., Maslennikov, V.V., Baker, M.J., Fox, N., Belousob, I., Figueroa, M.C., Steadman, J.A., Fabris, A.J., and Lyons, T.W., 2019, Distinguishing ore deposit type and barren sedimentary pyrite using laser ablation-inductively coupled plasma-mass spectrometry trace element data and statistical analysis of large data sets: Economic Geology, v. 114, p. 771–786.

Groves, D.I., Bierlein, F.P., Meinert, L.D., and Hitzman, M.W., 2010, Iron oxide copper-gold (IOCG) deposits through earth history: Implications for origin, lithospheric setting, and distinction from other epigenetic iron oxide deposits: Economic Geology, v. 105, p. 641–654.

Halley, S., 2020, Mapping magmatic and hydrothermal processes from routine exploration geochemical analyses: Economic Geology, v. 115, p. 489–503.

Hart, L., Wilkinson, J., Armstrong, R., and Araujo, D., 2017, Classifying propylitic alteration in complex porphyry systems; a case study of the Oyu Tolgoi Cu-Au porphyry deposits, Southern Mongolia, The IOCG-IOA Olympic Dam Cu-U-Au-Ag deposit and nearby prospects, South Australia: Society for Geology Applied to Mineral Deposits, Biennial Meeting, 14th, Québec City, Canada, 2017, Proceedings, p. 1081–1084.

Haynes, D.W., Cross, K.C., Bills, R.T., and Reed, M.H., 1995, Olympic Dam ore genesis: A fluid-mixing model: Economic Geology, v. 90, p. 281–307.

Hayward, N., and Skirrow, R.G., 2010, Geodynamic setting and controls on iron oxide Cu-Au (±U) ore in the Gawler Craton, South Australia, *in* Porter, T.M., ed., Hydrothermal iron oxide copper-gold and related deposits: A global perspective, v. 4: Porter GeoConsultancy Publishing, Adelaide, p. 1–27.

Hood, B.S., Cracknell, M.J., Gazley, M.F., and Reading, A.R., 2019, Element mobility and spatial zonation associated with the Archean Hamlet orogenic Au deposit, Western Australia: Implications for fluid pathways in shear zones: Chemical Geology, v. 514, p. 10–26.

Huang, Q., Kamenetsky, V.S., Ehrig, K., McPhie, J., Kamenetsky, M., Cross, K., Meffre, S., Agangi, A., Chambefort, I., Direen, N.G., Maas, R., and Apukhtina, O., 2016, Olivine-phyric basalt in the Mesoproterozoic Gawler silicic large igneous province, South Australia: Examples at the Olympic Dam iron oxide Cu-U-Au-Ag deposit and other localities: Precambrian Research, v. 281, p. 185–199.

Huang, X.-W., Sappin, A.-A., Boutroy, É., Beaudoin, G., and Makvandi, S., 2019, Trace element composition of igneous and hydrothermal magnetite from porphyry deposits: Relationship to deposit subtypes and magmatic affinity: Economic Geology, v. 114, p. 917–952.

Jagodzinski, E.A., 2005, Compilation of SHRIMP U-Pb geochronological data—Olympic Domain, Gawler Craton, South Australia, 2001–2003: Geoscience Australia, Canberra, 197 p.

Keyser, W., Ciobanu, C.L., Cook, N.J., Courtney-Davies, L., Kennedy, A., Wade, B.P., Ehrig, K., Dmitrijeva, M., Kontonikas-Charos, A., Feltus, H., and Johnson, G., 2019, Petrographic and geochronological constraints on the granitic basement to the Middleback Ranges, South Australia: Precambrian Research, v. 324, p. 170–193.

Keyser, W., Ciobanu, C.L., Cook, N.J., Wade, B.P., Kennedy, A., Kontonikas-Charos, A., Ehrig, K., Feltus, H., and Johnson, G., 2020, Episodic mafic magmatism in the Eyre Peninsula: Defining syn-and post-depositional BIF environments for iron deposits in the Middleback Ranges, South Australia: Precambrian Research, v. 337, p. 105535.

Kontonikas-Charos, A., Ciobanu, C.L., and Cook, N.J., 2014, Albitization and redistribution of REE and Y in IOCG systems: Insights from Moonta-Wallaroo, Yorke Peninsula, South Australia: Lithos, v. 208–209, p. 178–201.

Kontonikas-Charos, A., Ciobanu, C.L., Cook, N.J., Ehrig, K., Krneta, S., and Kamenetsky, V.S., 2017, Feldspar evolution in the Roxby Downs Granite, host to Fe-oxide Cu-Au-(U) mineralization at Olympic Dam, South Australia: Ore Geology Reviews, v. 80, p. 838–859.

——2018, Rare earth element geochemistry of feldspars: examples from Fe-oxide Cu-Au systems in the Olympic Cu-Au Province, South Australia. Mineralogy and Petrology, v. 112, p. 145–172.

Krneta, S., Ciobanu, C.L., Cook, N.J., Ehrig, K.J., and Kontonikas-Charos, A., 2017a, Rare earth element behaviour in apatite from the Olympic Dam Cu-U-Au-Ag deposit, South Australia: Minerals, v. 7, 26 p.

——2017b, The Wirrda Well and Acropolis prospects, Gawler Craton, South Australia: Insights into evolving fluid conditions through apatite chemistry: Journal of Geochemical Exploration, v. 181, p. 276–291.

Kuhn, S., Cracknell, M.J., and Reading, A.M., 2019, Lithological mapping in the Central African Copper Belt using Random Forests and clustering: Strategies for optimised results: Ore Geology Reviews, v. 111, article 103015.

Kuhn, S., Cracknell, M.J., Reading, A.M., and Sykora, S., 2020, Identification of intrusive lithologies in volcanic terrains in British Columbia by machine learning using random forests: The value of using a soft classifier: Geophysics, v. 85(6), p. 1–40.

Liaw, A., and Wiener, M., 2002, Classification and regression by randomForest: R News, v. 2, p. 18–22.

Mark, G., Oliver, N.H.S., and Williams, P.J., 2006, Mineralogical and chemical evolution of the Ernest Henry Fe oxide-Cu-Au ore system, Cloncurry district, northwest Queensland, Australia: Mineralium Deposita, v. 40, p. 769–801.

Mauger, A.J., Ehrig, K., Kontonikas-Charos, A., Ciobanu, C.L., Cook, N.J., and Kamenetsky, V.S., 2016, Alteration at the Olympic Dam IOCG-U deposit: Insights into distal to proximal feldspar and phyllosilicate chemistry from infrared reflectance spectroscopy: Australian Journal of Earth Sciences, v. 63, p. 959–972.

McPhie, J., Ehrig, K.J., Kamenetsky, M.B., Crowley, J.L., and Kamenetsky, V.S., 2020, Geology of the Acropolis prospect, South Australia, constrained by high-precision CA-TIMS ages: Australian Journal of Earth Sciences, v. 67, p. 699–716.

Montreuil, J.-F., Corriveau, L., and Grunsky, E.C., 2013, Compositional data analysis of IOCG systems, Great Bear magmatic zone, Canada: To each alteration types its own geochemical signature: Geochemistry: Exploration, Environment, Analysis, v. 13, p. 229–247.

O'Brien, J., Spry, P.G., Nettleton, D., Xu, R., and Teale, G.S., 2015, Using Random Forests to distinguish gahnite compositions as an exploration guide to Broken Hill-type Pb-Zn-Ag deposits in the Broken Hill domain, Australia: Journal of Geochemical Exploration, v. 149, p. 74–86.

Ordóñez-Calderón, J.C., and Gelcich, S., 2018, Machine learning strategies for classification and prediction of alteration facies: Examples from the Rosemont Cu-Mo-Ag skarn deposit, SE Tucson Arizona: Journal of Geochemical Exploration, v. 194, p. 167–188.

Parker, A.J., 1990, Gawler Craton and Stuart Shelf—regional geology and mineralization: Australasian Institute of Mining and Metallurgy, Monograph no. 14, p. 999–1008.

Paterson. H.L., 1986, The Acropolis prospect, in Paterson H.L.C., ed., Basement geology of the Stuart Shelf region, South Australia (vol. A1 – Olympic Dam/Stuart Shelf Excursion Guide, pp. 17–18). 8th Australian Geological Convention, Geological Society of Australia, Adelaide. Sydney, NSW.

Reeve, J.S., Cross, K.C., Smith, R.N., and Oreskes, N., 1990, Olympic Dam copper-uranium-gold-silver deposit: Australasian Institute of Mining and Metallurgy, Monograph no. 14, p. 1009–1035.

Reid, A., Hand, M., Jagodzinski, E., Kelsey, D., and Pearson, N., 2008a, Paleoproterozoic orogenesis in the southeastern Gawler Craton, South Australia: Australian Journal of Earth Sciences, v. 55, p. 449–471.

Reid, A.J., McAvaney, S.O., and Fraser, G.L., 2008b, Nature of the Kimban Orogeny across northern Eyre Peninsula: MESA Journal, v. 51, p. 25–34.

Skirrow, R.G., Bastrakov, E.N., Barovich, K., Fraser, G.L., Creaser, R.A., Fanning, C.M., Raymond, O.L., and Davidson, G.J., 2007, Timing of iron oxide Cu-Au-(U) hydrothermal activity and Nd isotope constraints on metal sources in the Gawler craton, South Australia: Economic Geology, v. 102, p. 1441–1470.

Skirrow, R.G., Van Der Wielen, S.E., Champion, D.C., Czarnota, K., and Thiel, S., 2018, Lithospheric architecture and mantle metasomatism linked to iron oxide Cu-Au ore formation: Multidisciplinary evidence from the Olympic Dam Region, South Australia: Geochemistry Geophysics Geosystems, v. 19, p. 2673–2705.

Vella, L., 1997, Interpretation and modelling, based on petrophysical measurements, of the Wirrda Well potential field anomaly, South Australia: Exploration Geophysics, v. 28, p. 299–306

Downloaded from http://pubs.geoscienceworld.org/segweb/economicgeology/article-pdf/117/4/853/5581376/4904_dmitrijeva_et_al.pdf
by China Geological Library user

Verdugo-Ihl, M.R., Ciobanu, C.L., Cook, N.J., Ehrig, K., Courtney-Davies, L., and Gilbert, S., 2017, Textures and U-W-Sn-Mo signatures in hematite from the Cu-U-Au-Ag orebody at Olympic Dam, South Australia: Defining the archetype for IOCG deposits: Ore Geology Reviews, v. 91, p. 173–195.

Verdugo-Ihl, M., Ciobanu, C.L., Cook, N.J., Ehrig, K., Slattery, A., and Courtney-Davies, L., 2020a, Trace element remobilisation from W-Sn-U-Pb zoned hematite: Nanoscale insights into a mineral geochronometer behaviour during interaction with fluids: Mineralogical Magazine, v. 84, p. 502–516.

Verdugo-Ihl, M.R., Ciobanu, C.L., Cook, N.J., Ehrig, K.J., and Courtney-Davies, L., 2020b, Defining early stages of IOCG systems: Evidence from iron oxides in the outer shell of the Olympic Dam deposit, South Australia: Mineralium Deposita, v. 55, p. 429–452.

Verdugo-Ihl, M.R., Ciobanu, C.L., Cook, N.J., Ehrig, K., Slattery, A., Courtney-Davies, L., and Dmitrijeva, M., 2021, Nanomineralogy of hydrothermal magnetite from Acropolis, South Australia: Genetic implications for iron-oxide copper gold mineralization: American Mineralogist, v. 106, p. 1273–1293.

Winderbaum, L., Ciobanu, C.L., Cook, N.J., Paul, M., Metcalfe, A.V., and Gilbert, S., 2012, Multivariate analysis of an LA-ICP-MS trace element dataset for pyrite: Mathematical Geosciences, v. 44, p. 823–842.

Marija Dmitrijeva is an exploration geologist specializing in the geochemistry of magmatic-hydrothermal ore deposits and applied statistical analysis of geochemical data. Marija finished her M.Sc. degree at the University of Tartu, Estonia, in 2015, and earned a Ph.D. from the University of Adelaide in 2020, where she worked on statistical analysis of geochemical data from the iron oxide copper-gold deposits in South Australia. In her spare time, she rides a road bike through the Adelaide Hills and enjoys salsa music.

Downloaded from http://pubs.geoscienceworld.org/segweb/economicgeology/article-pdf/117/4/853/5581376/4904_dmitrijeva_et_al.pdf
by China Geological Library user